

**TRANSIENT MICROSCOPY OF PRIMARY ATOMIZATION IN
GASOLINE DIRECT INJECTION SPRAYS**

A Thesis

Presented to

The Academic Faculty

by

Hussain Zaheer

In Partial Fulfillment

of the Requirements for the Degree

Master of Science in the

School of George W. Woodruff School of Mechanical Engineering

Georgia Institute of Technology

May 2015

Copyright © by Hussain Zaheer 2015

**TRANSIENT MICROSCOPY OF PRIMARY ATOMIZATION IN
GASOLINE DIRECT INJECTION SPRAYS**

Approved by:

Dr. Caroline Genzale, Advisor
George W. Woodruff School of Mechanical Engineering
Georgia Institute of Technology

Dr. Alexander Alexeev
George W. Woodruff School of Mechanical Engineering
Georgia Institute of Technology

Dr. S. Mostafa Ghiaasiaan
George W. Woodruff School of Mechanical Engineering
Georgia Institute of Technology

Date Approved: April 16th, 2015

*Dedicated to family, friends
and
a special person*

ACKNOWLEDGEMENTS

I would like to thank my advisor Dr. Caroline L. Genzale for her guidance, support and motivation without which I would never have been able to complete this work. It was her constant motivation and optimism that helped me carry on during the tough times and I am extremely grateful for it.

I would also like to thank my friends and SPheRe lab colleagues Benjamin Knox and Gina Magnotti who helped me get started with research and their continuous advice and inputs improved this work significantly.

I am also grateful for the help and support of my friends outside the lab which made my life at Tech so memorable and enjoyable.

Finally I would like to thank my parents, sisters and the entire family for believing in me, for giving me constant support, encouragement and prayers which kept me strong throughout the past two years.

TABLE OF CONTENTS

| | |
|--|------|
| ACKNOWLEDGEMENTS | iv |
| LIST OF TABLES | vii |
| LIST OF FIGURES | viii |
| LIST OF SYMBOLS AND ABBREVIATIONS | xi |
| SUMMARY | xiii |
| <u>CHAPTER</u> | |
| 1 INTRODUCTION | 1 |
| 2 LITERATURE REVIEW | 6 |
| 2.1 Experimental Investigation of High-Pressure Sprays | 8 |
| 3 EXPERIMENTAL SETUP | 15 |
| 3.1 Experimental Equipment | 15 |
| 3.1.1 High pressure and temperature combustion vessel | 15 |
| 3.1.2 Fuel Pump system | 16 |
| 3.1.3 GDI Injector | 18 |
| 3.1.4 Optical system design and characteristics | 18 |
| 3.1.5 Synchronization | 21 |
| 3.1.6 Complete experimental setup | 21 |
| 3.2 High Spatial and Temporal Imaging Tradeoffs | 22 |
| 3.2.1 Illumination – Magnification Trade-off | 23 |
| 3.2.2 Magnification – Field of view (FOV) Trade-off | 26 |
| 3.2.3 Framing rate – Field of view (FOV) Trade-off | 28 |

| | | |
|-------|--|----|
| 3.2.4 | Light pulse width – Illumination Trade-off | 29 |
| 3.3 | Illumination system setup | 31 |
| 3.3.1 | Optical power at the imaging plane | 37 |
| 3.3.2 | Image resolution quantification | 37 |
| 4 | RESULTS AND DISCUSSION | 42 |
| 5 | CONCLUSIONS AND FUTURE WORK | 54 |
| | REFERENCES | 58 |

LIST OF TABLES

| | Page |
|---|-------------|
| Table 1: Lens options for the design of the illumination system | 36 |
| Table 2: Pixel Size, magnification and size of FOV for 200 kfps and 480 kfps framing rate | 41 |

LIST OF FIGURES

| | Page |
|---|-------------|
| Figure 1: Breakup scales for high pressure fuel sprays at engine relevant conditions predicted by the Kelvin–Helmholtz breakup theory and Turbulent breakup theory. | 2 |
| Figure 2: Schematic diagram showing surface waves and breakup of a cylindrical liquid jet | 3 |
| Figure 3: Accurate sub-models are needed for detailed spray processes since drop sizes are much smaller than practical computer numerical grids | 4 |
| Figure 4: Cylindrical jet behavior | 7 |
| Figure 5: Shadowgraphic images showing effect of nozzle passage length on steady state jet breakup for water jets in a nitrogen environment at 300 psia and $\Delta p=1900$ psia (resolution $O[100 \mu\text{m}]$) | 9 |
| Figure 6: Pulsed Shadowgraphs of flow near the liquid surface at various distances from the jet exit for water injection into still air (resolution $O[10 \mu\text{m}]$) and Typical shadowgraphs of turbulent breakup | 10 |
| Figure 7: Hologram reconstruction of flow near the liquid surface at various relative velocities for water injection into still air (resolution $O[10 \mu\text{m}]$) | 11 |
| Figure 8: Example of the presence of a spheroidal cap and its evolution during the initial stage of fuel injection | 11 |
| Figure 9: Evidence of a liquid core immediately at the nozzle exit and Optical thickness measured with backlit microscopy overlaid with a derived optical thickness from the radiography measurements in light blue. | 12 |
| Figure 10: Diesel spray start of injection at low and high pressure and temperature ambient conditions | 13 |
| Figure 11: Location of sprays investigated in literature on the spray regime plot. | 14 |
| Figure 12: Schematic of the high pressure and temperature vessel and close-up of the combustion chamber. | 16 |
| Figure 13: Schematic of the bladder accumulator fuel pump system for GDI sprays. | 17 |
| Figure 14: Complete experimental setup schematic | 22 |

| | |
|---|----|
| Figure 15: The Numerical Aperture and F/# of a lens | 23 |
| Figure 16: Questar QM1 Short-Mount Long-Range Microscope Numerical Aperture and F/# vs Working Distance | 24 |
| Figure 17: Effect of adding additional magnification lens to the long-range microscope | 25 |
| Figure 18: Reduction in illumination intensity with increasing magnification | 25 |
| Figure 19: Reduction in FOV with increasing magnification | 27 |
| Figure 20: Reduction in maximum feature velocity for capturing 3 frames in FOV with increasing magnification | 28 |
| Figure 21: Reduction in FOV with increasing frame rate (the data labels show dimension of FOV in pixels) | 29 |
| Figure 22: Maximum feature velocity for a given exposure duration to avoid blur | 31 |
| Figure 23: Viewing cone of the Questar QM1 short mount long-range microscope | 32 |
| Figure 24: Optical ray trace for a single lens showing the maximal ray | 33 |
| Figure 25: Schematic for the two lens system for the illumination setup | 34 |
| Figure 26: The product of spot size and f/# for the lens choices | 36 |
| Figure 27: Final schematic of the illuminating system with focal lengths and diameters of the lenses and the size of the source and image | 36 |
| Figure 28: Optical power measured at the spray plane by PDA36A – Si Switchable Gain Detector | 37 |
| Figure 29: High contrast periodic grating and Image of the high contrast periodic grating | 38 |
| Figure 30: Periodic gratings with their contrast and Images of these periodic gratings with their contrast | 39 |
| Figure 31: 1951 USAF test target for MTF calculation | 40 |
| Figure 32: Modulation Transfer Function of the designed optical system | 41 |
| Figure 33: Shadowgraph of the whole spray at atmospheric temperature and pressure and 3000 psi injection pressure | 42 |

| | |
|--|----|
| Figure 34: Microscopic images of the spray at 21 MPa (3000 psi) injection pressure. 2.9x magnification, 200 kfps framing rate and 90 ns exposure. | 43 |
| Figure 35: Microscopic images of the spray at 21 MPa (3000 psi) injection pressure. 13.7x magnification, 200 kfps framing rate and 90 ns exposure. | 44 |
| Figure 36: Microscopic images of the spray at 21 MPa (3000 psi) injection pressure, 2.9x Magnification, 480 kfps framing rate and 20 ns exposure. | 45 |
| Figure 37: Microscopic images of the spray at 6.9 MPa (1000 psi) injection pressure, 2.9x Magnification, 200 kfps framing rate and 90 ns exposure. | 46 |
| Figure 38: Microscopic images of the spray at 6.9 MPa (1000 psi) injection pressure, 13.7x Magnification, 200 kfps framing rate and 90 ns exposure. | 47 |
| Figure 39: Microscopic images of the spray at 6.9 MPa (1000 psi) injection pressure, 2.9x Magnification, 480 kfps framing rate and 20 ns exposure. | 48 |
| Figure 40: Microscopic images of the spray at 1.4 MPa (200 psi) injection pressure, 2.9x Magnification, 200 kfps framing rate and 90 ns exposure. | 49 |
| Figure 41: Microscopic images of the spray at 1.4 MPa (200 psi) injection pressure, 13.7x Magnification, 200 kfps framing rate and 90 ns exposure. | 50 |
| Figure 42: Microscopic images of the spray at 1.4 MPa (200 psi) injection pressure, 13.7x Magnification, 480 kfps framing rate and 20 ns exposure. | 51 |
| Figure 43: Microscopic images of the spray at 1.4 MPa (200 psi) injection pressure, 13.7x Magnification, 480 kfps framing rate and 90 ns exposure. | 52 |
| Figure 44: Microscopic images of the spray at 1.4 MPa (200 psi) injection pressure. 2.9x Magnification, 200 kfps framing rate and 90 ns exposure at 1 MPa ambient pressure | 53 |
| Figure 45: Comparison of sprays investigated in current work with sprays investigated in literature on the spray regime plot. | 56 |

LIST OF SYMBOLS AND ABBREVIATIONS

Symbols

| | |
|-----------|-------------------|
| Re | Reynolds Number |
| We | Weber Number |
| ρ | Density |
| U | Velocity |
| d | Orifice Diameter |
| λ | Wavelength |
| μ | Dynamic viscosity |
| σ | Surface tension |
| L | Length |
| $F/\#$ | f-number |

Subscripts

| | |
|-----|--------|
| L | Liquid |
| G | Gas |

Abbreviations

| | |
|-------|------------------------------|
| CFD | Computational Fluid Dynamics |
| GDI | Gasoline Direct Injection |
| MTF | Modulation Transfer Function |
| FOV | Field of View |
| LED | Light Emitting Diode |
| MP | Megapixels |

CMOS Complementary metal–oxide–semiconductor
NA Numerical Aperture
USAF United States Air Force

SUMMARY

Understanding the physics governing primary atomization of high pressure fuel sprays is of paramount importance to accurately model combustion in direct injection engines. The small length and time scales of features that characterize this process falls below the resolution power of typical grids in CFD simulations, which necessitates the inclusion of physical models (sub-models) to account for unresolved physics. Unfortunately current physical models for fuel spray atomization used in engine CFD simulations are based on significant empirical scaling because there is a lack of experimental data to understand the governing physics. The most widely employed atomization sub-model used in current CFD simulations assumes the spray atomization process to be dominated by aerodynamically-driven surface instabilities, but there has been no quantitative experimental validation of this theory to date. The lack of experimental validation is due to the high spatial and temporal resolutions required to simultaneously to image these instabilities, which is difficult to achieve.

The present work entails the development of a diagnostic technique to obtain high spatial and temporal resolution images of jet breakup and atomization in the near nozzle region of Gasoline Direct Injection (GDI) sprays. It focuses on the optical setup required to achieve maximum illumination, image contrast, sharp feature detection, and temporal tracking of interface instabilities for long-range microscopic imaging with a high-speed camera. The resolution and performance of the imaging system is characterized by evaluating its modulation transfer function (MTF). The setup enabled imaging of GDI sprays for the entire duration of an injection event (several milliseconds) at significantly

improved spatial and temporal resolutions compared to historical spray atomization imaging data. The images show that low to moderate injection pressure sprays can be visualized with a high level of detail and also enable the tracking of features across frames within the field of view (FOV).

CHAPTER 1: INTRODUCTION

In recent years, the growing environmental concerns related to global warming and climate change has focused the attention of researchers on the development of energy efficient technologies to reduce greenhouse gases emission into the environment. Governments across the world are also setting directives to facilitate the development of efficient technologies. Since 56% of the world's liquid fuel consumption is being used in the transportation sector [1], efficient combustion of liquid fuels in internal combustion engines will have a significant contribution towards controlling the emission of greenhouse gases.

Understanding the processes that govern the combustion of liquid fuels in internal combustion engines is the first step in increasing their efficiency. The combustion of liquid fuels starts with the preparation of an air fuel mixture. Although many mechanisms exists for preparing this mixture, the predominant mechanism for diesel engines, and recently for gasoline engines with GDI (Gasoline Direct Injection) technologies, involves the injection of high-pressure liquid fuel sprays into a high-pressure gaseous environment. However, the fundamental physics that govern the primary breakup and atomization of these high pressure sprays into dense engine-like environments are poorly understood because of the extreme conditions in which this process occurs. These conditions are characterized by the injection of high pressure liquids, in the range of 100-3000 bar, into dense environments with gas density ranging from 10-50 kg/m³, which results in flows having liquid Reynolds numbers ($Re_L = \rho_L U_L d / \mu_L$) in the range of 10⁴-10⁵ and Weber numbers ($We = \rho_L U_L^2 d / \sigma$) in the range of 10⁴-10⁶. The characteristic

dimension of interfacial instabilities and droplets formed from these flows are typically in the range of microns as shown in Figure 1 and they are moving at velocities of hundreds of meters per second. These extreme spatial and temporal scales are challenging to characterize both experimentally and computationally.

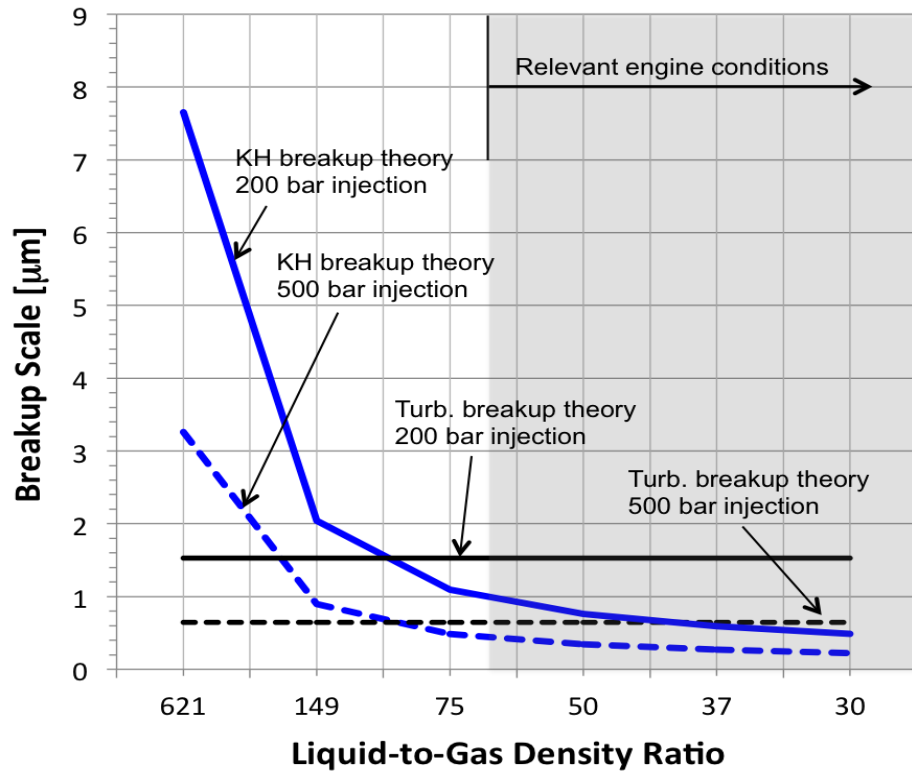


Figure 1: Breakup scales for high pressure fuel sprays at engine relevant conditions predicted by the Kelvin–Helmholtz breakup theory and Turbulent breakup theory.

The inability to form a comprehensive theoretical model for primary atomization in fuel sprays, despite numerous experimental and theoretical studies (e.g., [2][3][4][5][6]), also arises from the fact that spray atomization has been shown qualitatively to depend on a large number of parameters, including nozzle flow [7], nozzle cavitation [8], ambient conditions [7], fluid physical properties [9], and the effects of liquid turbulence [10]. Without experimental data to quantify the relative importance

of these parameters, a robust physical description of fuel spray atomization has yet to be developed. Current theoretical models for diesel spray atomization are based on the premise that aerodynamically-induced instabilities dominate the process [11]. As shown in Figure 2, this theory is based on linear instability analysis, where the fastest growing surface wave, with wavelength Λ , leads to droplets with characteristic sizes that scale with Λ . The influences of nozzle internal flow is only included empirically in such models, but these effects are known to be important for high pressure sprays. Moreover, the effect of liquid flow turbulence has been shown qualitatively [10][12][13], but its quantitative contribution is yet to be determined.

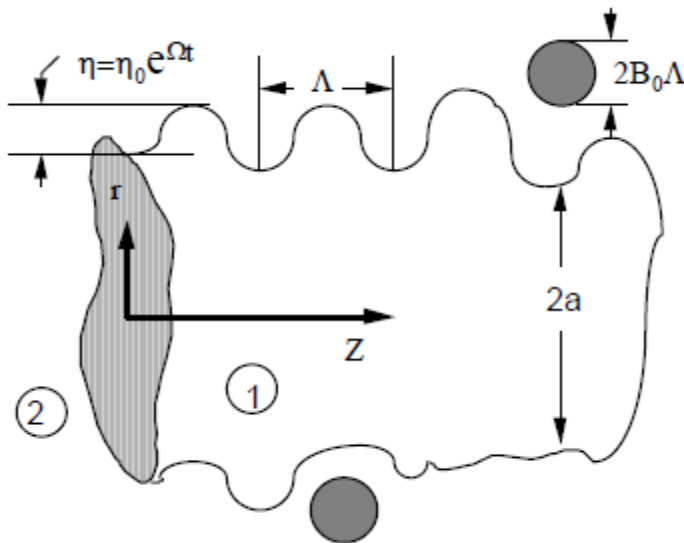


Figure 2: Schematic diagram showing surface waves and breakup of a cylindrical liquid jet [14]

Current computer models for engine combustion must solve conservation equations for the transient dynamics of vaporizing fuel sprays, which interact with multicomponent gases and undergo mixing, ignition, chemical reactions, and heat transfer in arbitrary shaped (moving) geometries. Due to the wide range of length and

time scales that characterize these processes and limitations of current computing capabilities, many of the governing physics fall in the sub-grid scale. For example, in a 3-dimensional finite-difference computation, to begin to resolve the flow-field around $10\ \mu\text{m}$ diameter drops (typical of the drop Sauter mean diameter in combustion applications) in a 10 cm diameter combustion chamber requires about 10^{12} grid points (see Figure 3). Due to limitations of computer storage and run times, a practical upper-limit for current super-computers is about 10^5 grid points. The missing 7 orders of magnitude will not be realized in the next decade, even with the most optimistic projections about computer power increases. This necessitates the inclusion of a theoretical model, or sub-model, to describe the unresolved spray atomization physics in engine CFD simulations which inherently brings empiricism into the simulation and limits its predictive capability [11].

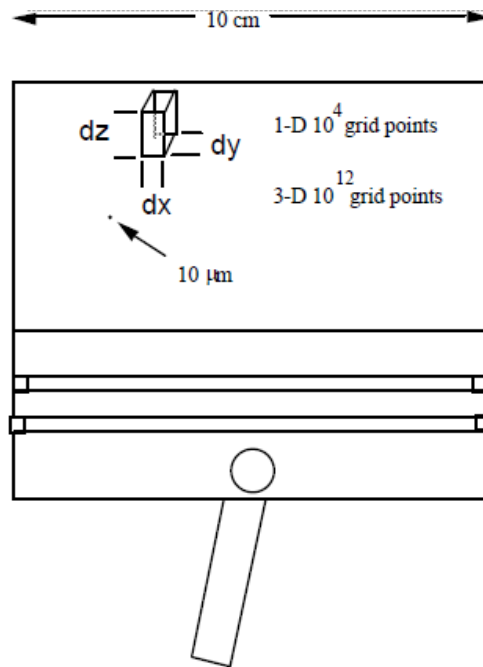


Figure 3: Accurate sub-models are needed for detailed spray processes since drop sizes are much smaller than practical computer numerical grids [14]

The experimental data on which current sub-models [2] have been based are significantly lacking in quantitative resolution. Historical imaging data are limited by the imaging technology of that time, resulting in under-resolved spatial resolution and single-shot still frame images that greatly limit the ability to quantify interfacial instabilities, their growth histories, and the resulting atomization outcomes. Furthermore, the region of primary breakup for high-pressure sprays is optically very dense, which limits the penetration of light through it using conventional lightening techniques. Hence, quantitative drop sizing measurement techniques are not feasible in these regions. Recent advances in high-speed imaging technology, in conjunction with long-range microscopy and short pulsed LED illumination, provides new tools to image sprays at the extremely challenging micrometer spatial scales and nanosecond time scales. The present work develops a transient microscopy diagnostic technique to image GDI sprays at the maximum spatial and temporal resolution possible using state-of-the-art technologies and also determines the spray operating conditions where the primary breakup process can be temporally and spatially resolved with the designed imaging system. The aim of this diagnostic development effort is to enable the quantitative description of interfacial instabilities, how they evolve with time, and how it results in primary atomization. Resolution of these processes should lead to the reduction or elimination of empiricism from sub-models in CFD simulations, which will greatly increase their predictive capability. Accurate prediction of direct fuel injection for engine CFD simulations will enable a broader investigation of new high-efficiency lean-burn low temperature combustion strategies and also give better insight into using bio-fuels, which have significantly different physical properties as compared to conventional fossil fuel.

CHAPTER 2: LITERATURE REVIEW

The formation of liquid sprays has been classically theorized to follow a sequence of the following three steps: (i) ejection of liquid flow into a gaseous environment (ii) primary breakup and (iii) secondary breakup. The intermediate step of primary atomization, which constitutes initial flow deformations and the subsequent production of liquid fragments from these deformations, is extremely important to understand because it provides a link between the flow issuing from the atomizer and the spray morphology. For high-pressure fuel sprays, this step plays a vital role in combustion process and emission formations since these processes are highly dependent on the air-fuel mixtures that are governed by the primary atomization mechanism. Widely used theoretical models of the initial breakup of liquid sprays in high ambient density environments have been based on the hypothesis that unstable waves develop and grow on the liquid-gas interface and dominate its breakup [15]. However, a coupling of the processes upstream in the nozzle with the wave development phenomenon downstream is also required as it has been shown to play an important role in the primary atomization mechanism of high-pressure sprays [2]. Unfortunately, there has been no consensus on the correct theoretical description of atomization for high-pressure sprays due to a lack of resolved experimental data. The experimental verification of these theoretical models have been done by comparison with measurements of large scale spray characteristics (cone angle, breakup length and mean drop diameter) where the primary atomization process is unresolved due to the inability of the employed diagnostics to quantify it.

High-pressure fuel sprays fall under the broad category of cylindrical liquid jets which are defined as sprays produced by forcing a liquid through a cylindrical tube of diameter d and length L . These sprays can be further divided into sub-regimes based on the disintegration mechanism observed, which can be expressed as a function of the liquid Reynolds number and Weber number. A jet stability curve is commonly used to categorize these sub-regimes based on the liquid breakup length, L_{BU} , and the average exit velocity of the liquid, U_L [15]. The breakup length is the length of the continuous jet attached to the nozzle and the average exit velocity of the liquid is defined as the volume flow rate of the liquid divided by the cross-sectional area of the nozzle orifice. Based on the above criteria of classification, five breakup regimes have been identified, known as the dripping regime (region A), the Rayleigh (region B), the first wind-induced (region C), the second wind-induced (region D), and the atomization (region E) regimes, as shown in Figure 4.

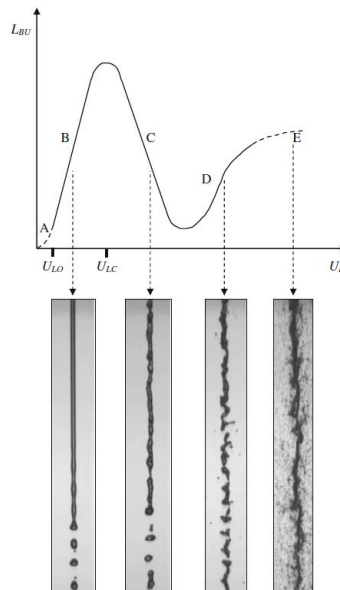


Figure 4: Cylindrical jet behavior. Top stability curve, bottom example of visualizations (from left to right): Rayleigh regime (region B) $Re_L = 790$, $We_G = 0.06$; first wind-induced regime (region C) $Re_L = 5,500$, $We_G = 2.7$; second wind-induced regime (region D) $Re_L = 16,500$, $We_G = 24$; atomization regime (region E) $Re_L = 28,000$, $We_G = 70$ [15]

High-pressure fuel sprays lie in the atomization regime, which has been characterized by the observation of complete jet disruption at the nozzle exit, producing average drop diameters much less than the jet diameter. It has also been shown that the onset of breakup in this regime is strongly influenced by the degree of flow development, turbulence and cavitation [13].

2.1 Experimental Investigation of High-Pressure Sprays

Reitz and Bracco [2][7] conducted an extensive experimental validation of their unstable wave growth theory for the primary atomization of high-pressure fuel sprays. The theory and models developed from that work [2][7] are now used in nearly all engine CFD codes to model the primary atomization of direct-injection fuel sprays [11]. Images were obtained using shadowgraphy, which is one of the most popular flow visualization techniques for sprays. It uses the principle that when back-illuminating a flow, disturbances in the medium refracts and scatters light rays, casting shadows that are imaged as dark objects against an illuminated backdrop. The images obtained by Reitz and Bracco were limited in their spatial resolution ($O[100 \mu\text{m}]$) and had no temporal resolution, as shown in Figure 5. They validated their primary breakup model indirectly using large-scale spray parameters, such as spray spreading angle, from ensemble-averaged data [7]. Another indirect quantitative validation of the unstable wave growth model was performed via drop size measurements far downstream of the jet exit [3]. Since these validations were based on indirect measurements, they required empirical scaling to match the predictions of the theoretical model. It was concluded from these validations that the aerodynamic surface wave growth mechanism cannot fully explain

the process of primary atomization and the contributions of other factors, such as nozzle internal flow, turbulence, and cavitation, should also be taken into account

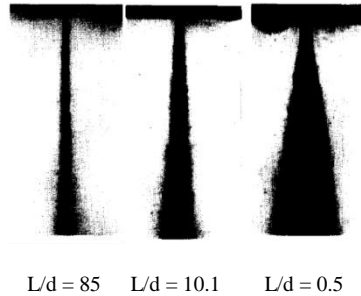


Figure 5: Shadowgraphic images showing effect of nozzle passage length on steady state jet breakup for water jets in a nitrogen environment at 300 psia and $\Delta p=1900$ psia (resolution $O[100 \mu\text{m}]$)[2]

More recently, Wu et al. [5] and Sallam et al. [13][10] investigated the formation of ligaments and drops at the liquid surface during primary breakup of turbulent liquid jets using single- and double-pulse shadowgraphy and single-pulse off-axis holography as shown in Figure 6. Shadowgraphy was performed using lasers, which gave the capability of a 7 ns exposure separated by 100 ns. The single pulse resulted in still images whereas the double-pulse yielded two images 100 ns apart. The spatial resolution they achieved in the shadowgraphy images allowed objects as small as 5 μm to be observed and as small as 10 μm to be measured with 10% accuracy. However, the formation and growth history of the ligaments could not be well evaluated because of the limited temporal data available with this technique. Shadowgraphy was used for flow visualization and to measure liquid surface velocities, properties at the onset of ligament and drop formation, and drop and ligament properties along the liquid surface.

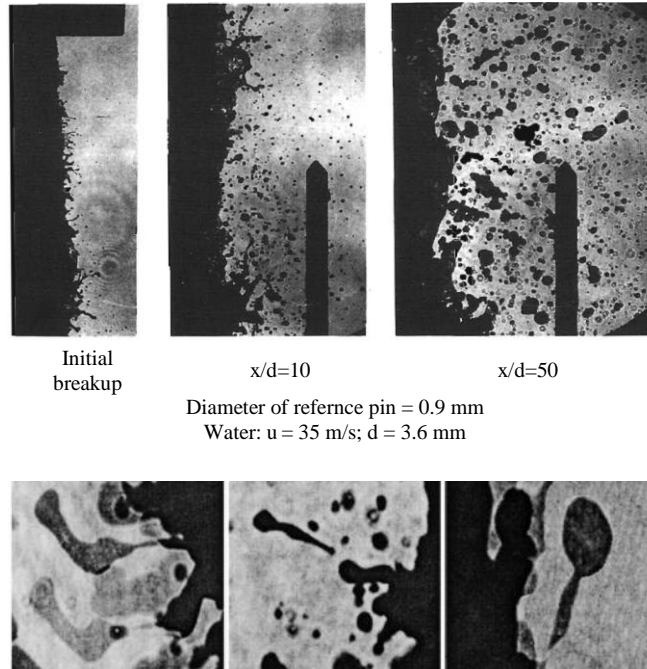


Figure 6: [Top] Pulsed Shadowgraphs of flow near the liquid surface at various distances from the jet exit for water injection into still air (resolution $O[10 \mu\text{m}]$) [5] and [Bottom] Typical shadowgraphs of turbulent breakup [10]

Single-pulse off-axis holography yielded still holograms (no temporal resolutions) of the liquid surface with spatial resolutions capable of observing $5 \mu\text{m}$ diameter drops and measuring $10 \mu\text{m}$ diameter drops with 10% accuracy. These holograms as shown in Figure 7 were used to measure drop liquid flux distributions along the liquid surfaces. Their conclusions suggested that the onset of ligament formation was associated with the convection of turbulent eddies within the liquid jet along the liquid-gas interface, which stands in contrast to the principles of the wave growth model of Reitz and Bracco. However, the liquid-to-gas density ratios at which these experiments were performed (e.g. $\rho_L/\rho_g = 690$ to 860) are significantly higher than those at engine relevant conditions ($\rho_L/\rho_g < 60$), which restricts the applicability of these results for fuel injection processes.

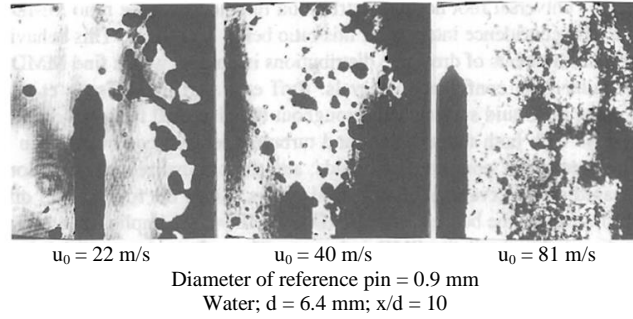


Figure 7: Hologram reconstruction of flow near the liquid surface at various relative velocities for water injection into still air (resolution $O[10 \mu\text{m}]$)[5]

The development of long-range microscopy has enabled researchers to achieve imaging resolution close to the diffraction limit. Crua et al [16] and Shoba et al [17] combined high speed imaging with long-range microscopy using pulsed lasers to achieve sub-micron spatial resolution. However the temporal data for this imaging technique was limited to still images or a maximum of 16 frames at a rate of $2\mu\text{s}$ per frame. These limitations restricted their work to focus on the relatively slow initial transient phase of injector opening as shown in Figure 8 and they did not focus on imaging primary atomization.

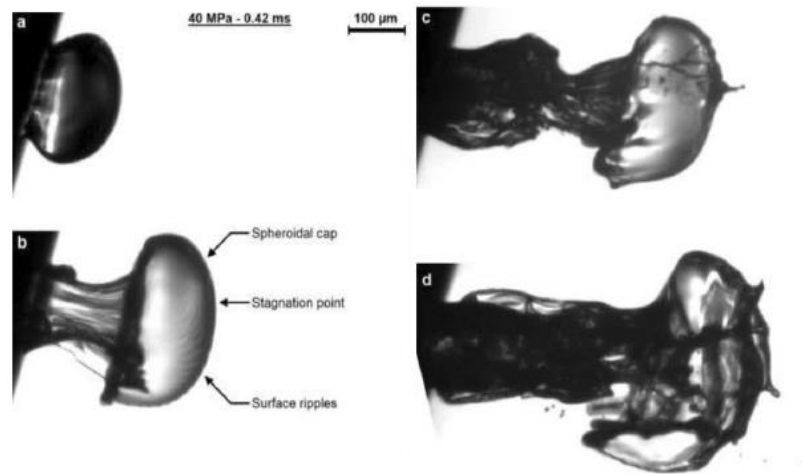


Figure 8: Example of the presence of a spheroidal cap and its evolution during the initial stage of fuel injection [16]

The latest developments in pulsed LEDs have enabled their use as a viable light source for high-speed imaging. Their high optical power (1-2 W), combined with a short pulse width capability (10-20 ns), and a high repetition rate (0.1 to 0.5 MHz), has enabled the imaging of high-speed sprays at high temporal resolution for the entire duration of a fuel injection event (2-3 ms). Recent work by Pickett et al [18] utilized pulsed LEDs as the light source for diffused back illumination imaging, using long-range microscopy, of the near-field structure and growth of a diesel spray. They achieved a spatial resolution of $4.7 \mu\text{m}/\text{pixel}$ at an image acquisition speed of 156,000 frames per second (fps) with a 1.4 mm long field of view (FOV). These achievements in spatial and temporal resolution indicate new potential for resolving primary breakup in practical fuel sprays. Their images (see Figure 9) indicate the presence of a pure liquid core immediately at the nozzle exit, suggesting that a finite time for interface instability growth is required to completely disrupt the issuing liquid jet.

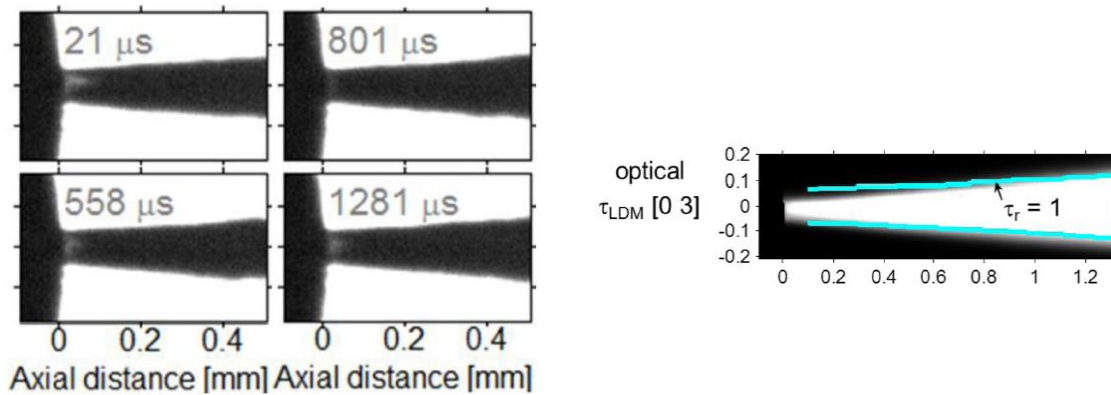


Figure 9: [Left] Evidence of a liquid core immediately at the nozzle exit [Right] Optical thickness measured with backlit microscopy overlaid with a derived optical thickness from the radiography measurements in light blue [18].

Manin et al. [19] used long-range microscopy to investigate primary atomization of diesel sprays injected into high temperature and pressure conditions. Pulsed LEDs were also used as the light-source for the diffused back illumination imaging using long-range microscopy in this work. Their images as shown in Figure 10 found the presence of droplets and ligament dynamics at low pressure and temperature ambient conditions, but not at high pressure and temperature conditions that are relevant for engine conditions. They attributed the lack of observed droplet dynamics to reduced surface tension effects at the gas-liquid interface, due to the supercritical nature of the air-fuel mixture that could be present at these high pressure and temperature conditions. However, the lack of evidence of droplets and ligaments may also be attributed to the inability of the optical system to resolve these features, both spatially and temporally. The occurrence of supercritical mixtures in engine fuel sprays needs to be verified further by completely eliminating uncertainties due to image focusing and resolution.

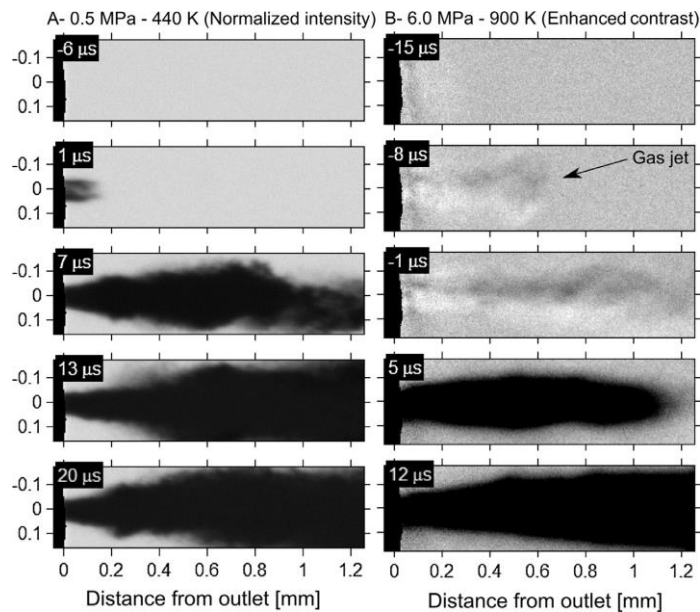


Figure 10: Diesel spray start of injection at low [Left] and high [Right] pressure and temperature ambient conditions [19]

Figure 11 shows the location of sprays that were investigated in literature on the regime plot where the regimes are the same that were specified in Figure 4. It can be seen from this figure that the highly resolved sprays by Sallam and Faeth are in the low pressure sprays regime (2nd Wind induced regime) whereas the high pressure spray investigation by Reitz and Bracco and Manin et al. is not highly resolved. Hence this is another proof of the lack of high resolution data for high pressure fuel sprays because of the challenging temporal and spatial scales required for these sprays.

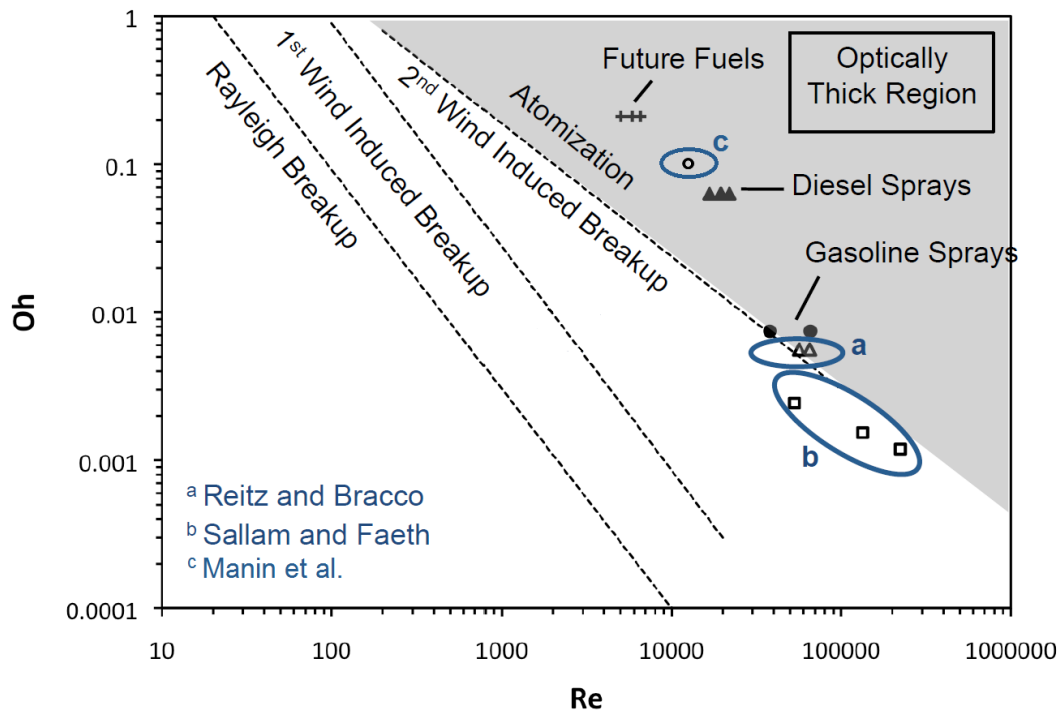


Figure 11: Location of sprays investigated in literature on the spray regime plot.

CHAPTER 3: EXPERIMENTAL SETUP

The transient microscopy of primary atomization in GDI fuel sprays was performed in an optically accessible high pressure and temperature combustion vessel. The fuel delivery and optical system was also designed to perform the microscopic imaging. This chapter describes each of these systems and equipment in detail.

3.1 Experimental Equipment

3.1.1 High pressure and temperature combustion vessel

The Spray Physics and Engine Research lab at the Georgia Institute of Technology is equipped with a state of the art optically-accessible high pressure and temperature combustion vessel. Figure 12 (a) shows the schematic of the whole vessel with Figure 12 (b) showing the close-up of the combustion chamber and the location of the spray. A wide range of operating conditions can be simulated in the vessel (up-to 100 bar and 900 K) which includes most of the gasoline and diesel engine operating conditions. The vessel design consists of two concentric cylindrical chambers; the inner chamber is insulated from the outer chamber to isolate the high-temperature air flow from the pressure-bearing windows. A continuous flow of air passes through the vessel, with pressurized air fed to the vessel from the bottom inlet, which passes through two cylindrical 15 kW heaters and a disc shaped 5 kW heater in the chamber to raise its temperature to the desired operating point. The diffuser at the entrance of the inner chamber distributes the air to provide a quasi-uniform temperature environment. The velocity of the air flow in the chamber is negligible as compared to the velocity of the

spray and thus the ambient environment can be assumed to quiescent. The temperature of the injector is kept constant by cooling water which circulates inside the injector holder. The vessel is optically accessible from the two sides, the front (not shown) and the top by means of fused silica windows.

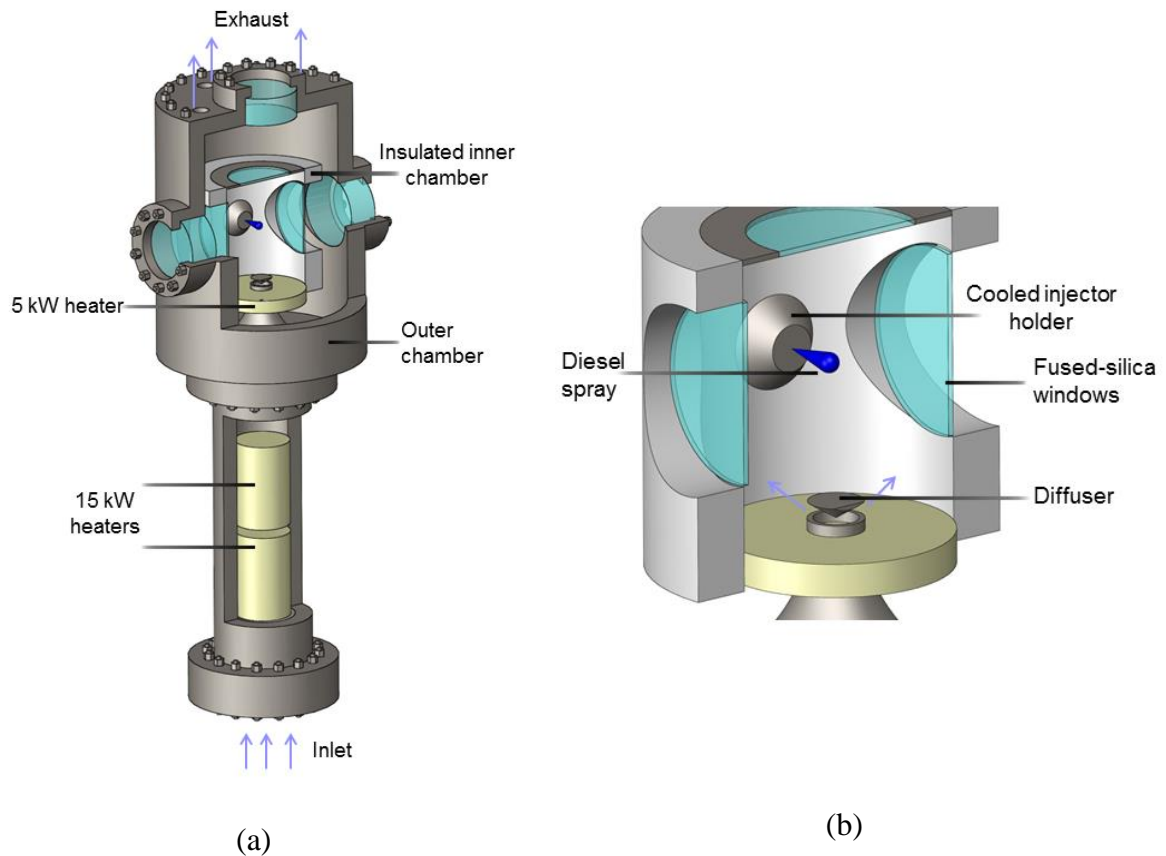


Figure 12: (a) Schematic of the high pressure and temperature vessel (b) close-up of the combustion chamber.

3.1.2 Fuel Pump system

GDI fuel sprays work at lower pressures (10-60 MPa) as compared to diesel sprays (~ 500 MPa), which enables the use of a static pump. The advantage of using a static design is that it eliminates pressure fluctuations which are inherent in a dynamic system. The static fuel system was designed based on a bladder accumulator with a

maximum operating pressure of 3000 psi (~ 20 MPa). Figure 13 shows a schematic of the fuel system. High pressure nitrogen from a nitrogen cylinder is fed to the nitrogen side of the accumulator, which expands the diaphragm and pressurizes the fuel side of the accumulator. Iso-octane (C_8H_{18}) is used as the fuel for all experiments. Iso-octane was selected as a representative liquid fuel for GDI sprays because, as a single-component fuel, it has well defined physical properties. It is also a representative component of real gasoline fuels. The diaphragm of the bladder is made of Viton and is fully compatible with a wide range of fuels. The inert nature of nitrogen made it the most suitable choice for use as the pressurizing medium. A fuel charging tank is used to fill the fuel side of the bladder using pressurized air. Using air in this part of the system was acceptable since it is at a very low pressure of around 80 psi (~ 0.5 MPa) and is only used when the fuel system requires refilling.

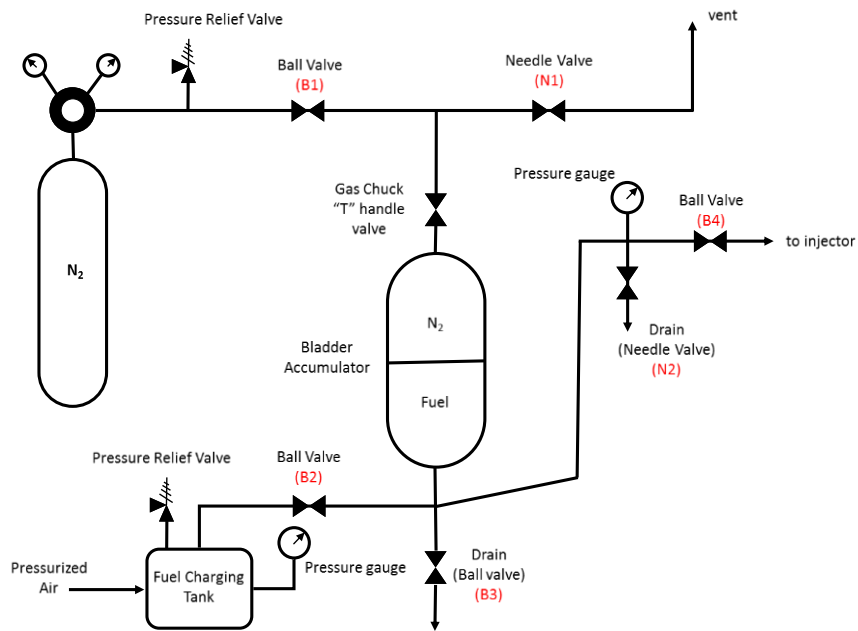


Figure 13: Schematic of the bladder accumulator fuel pump system for GDI sprays.

3.1.3 GDI Injector

A solenoid-actuated Magneti Marelli GDI injector with 5 counter-bored nozzle orifices was used to perform this study. The nominal diameter of the inner holes of the counter bore is 125 microns. Four holes of the injector are arranged in a V-shaped pattern with the fifth hole at the top of the 'V'. The injector is oriented in the vessel in such a way that the jet from the fifth hole emanates horizontally whereas the other four jets move diagonally upwards (see Figure 33). This allows imaging of the fifth jet without interaction from the other four. The injection pressures for the tests were varied from 1.4 to 21 MPa (200 to 3000 psi).

3.1.4 Optical system design and characteristics

The design of the optical system is the most critical part of the experimental setup. As explained in the introduction, the spatial and temporal resolution required to image high pressure sprays are extremely challenging and the optical system needs to be designed accordingly to be able to meet these extreme requirements. Past research on primary atomization of sprays has struggled to achieve the high spatial and temporal resolutions simultaneously, as discussed in the literature review.

The optical system consists of three parts, (i) Camera for imaging the sprays (ii) Long-range microscopic lens to visualize the microscopic details of the spray and (iii) the lighting system to illuminate the spray.

(i) High-Speed Camera

Past research on imaging of primary atomization has used both still-frame and high-speed cameras [16][19]. The advantage of using still-frame cameras is the higher

imaging resolution that can be achieved, with current scientific-grade CCD cameras offering resolutions as high as 16 megapixels, but these cameras cannot inherently provide any temporal resolution [16]. High-speed cameras provide the capability to temporally resolve the spray motion, but at the expense of imaging resolution [19]. The latest technologies in high-speed CMOS cameras only have a maximum imaging resolution of 1 megapixel (MP) at a maximum framing rate of 13,500 frames-per-second (fps). In addition, the resolution decreases as the framing rate is increased to higher values. In the current optical system design a Photron Fastcam SA-X2 high-speed camera is used to enable good temporal resolution of the spray. The Photron Fastcam SA-X2 has a state-of-the-art 1-MP CMOS sensor with 20 μm square pixels and 12-bit recording capability. The SA-X2 can reach framing speeds of up to a million fps and a minimum 1- μs shutter. Note that at this imaging speed, the imaging resolution is only 128 x 8 pixels. The inherent trade-offs in temporal and spatial resolution when utilizing a high-speed camera such as the SA-X2 are discussed in further detail in Section 3.2.

(ii) Long-Range Microscopic Lens

The microscopic details of the spray are visualized by QM 1 Short Mount Long-Distance Microscope. The QM1 has a working range of 560 mm (22 in) to 1520 mm (66 in) and a clear aperture of 89 mm (3.5 in). The f/no (ratio of focal length to diameter of the lens) of the QM1 varies from 8.7 at 560 mm to 16.8 at 1400 mm and has a manufacturer specified maximum optical resolution of 3 microns at 22 inches.

(iii) Light sources

A powerful light source is required to meet the illumination challenges of high-speed imaging since higher imaging frame rates provide less time for light integration at the camera sensor, which reduces the recorded intensity of the image. However, power is not the only requirement desired in a light source to be used for ultra-high-speed imaging applications such as the current work. As will be explained later, even the fastest shutter speed available with the SA-X2 (1 μ s) is not enough to freeze the motion of high-pressure fuel sprays in the frame. Thus, a pulsed light source is required to freeze the spray by acting as an optical shutter. Lasers are by far the most powerful light sources available, but they are somewhat limited in their capacity to be repetitively pulsed. The fastest repetition rate for commercially-available lasers is currently near 10 kHz.

In the current work, newly available high-power pulsed LEDs are explored as a light source. They have the capability to be overdriven when being pulsed, providing high optical powers in the range of 1-1.5 W, with pulses as short as 20 ns and pulse repetition-rates ranging from 0.1 to 0.5 MHz. The short pulse duration is on the order of typical laser pulse durations (\sim 10 ns), enabling maximum potential to freeze the motion of the spray in each frame, but with the added benefit of a high pulse repetition-rate to enable the acquisition of many frames throughout the entire duration of a fuel injection event (a few milliseconds). In the current experimental setup, a high powered pulsed LED system from LightSpeed Technologies is used. The setup uses a white LED (5500 K), which provides an optical power output near 1 W. The pulsed LED driver from LightSpeed (HPLS-DD18B) enabled pulsed flashes at 18 Amps for a maximum duty of 1% (e.g. a 100 ns pulse can have a maximum 0.1 MHz repetition rate), whereas the

maximum current that can be used in continuous-illumination mode is only 0.5 Amps. Another advantage of using a broadband LED over coherent and narrowly monochromatic lasers is that the back-illuminated images are free from speckle artifacts [20].

3.1.5 Synchronization

High speed imaging with camera framing rates in the range of 0.1 – 0.5 MHz and LED pulsing at the same rate requires precise synchronization of both systems. In addition to this, the start of both systems needs to be synchronized with the injection event. The Model 577 digital delay/pulse generator from Berkley Neucleonics Corporation was used to perform this synchronization. The Model 577 has a 5 ns resolution of the internal rate generator with a less than 500 ps RMS jitter and can provide 250 ps resolution for each individual channel. The signal for the start of injection was recorded using a Pearson Model 110 current monitor and sent to the pulse generator to trigger the camera recording and the LED pulsing.

3.1.6 Complete experimental setup

The schematic of the complete experimental setup is shown in Figure 14. The design of the illumination system which includes the condenser lens and the fresnel lens shown in the schematic is explained in section 3.3. The spray is illuminated using back-illumination where it is imaged as a dark shadow in a bright background. The spray refracts light differently than the ambient air in the chamber and hence casts a shadow which can be visualized against an illuminated background. The fuel pump supplies pressurized fuel to the injector and the operation of the injector is controlled by the injector driver. An injection signal from the injector driver opens the injector and is

simultaneously recorded by the current monitor which in turn sends a trigger signal to the digital delay generator. The digital delay generator uses this trigger to activate the LED pulsing and the high-speed camera recording and the back-illuminated images of the spray are obtained.

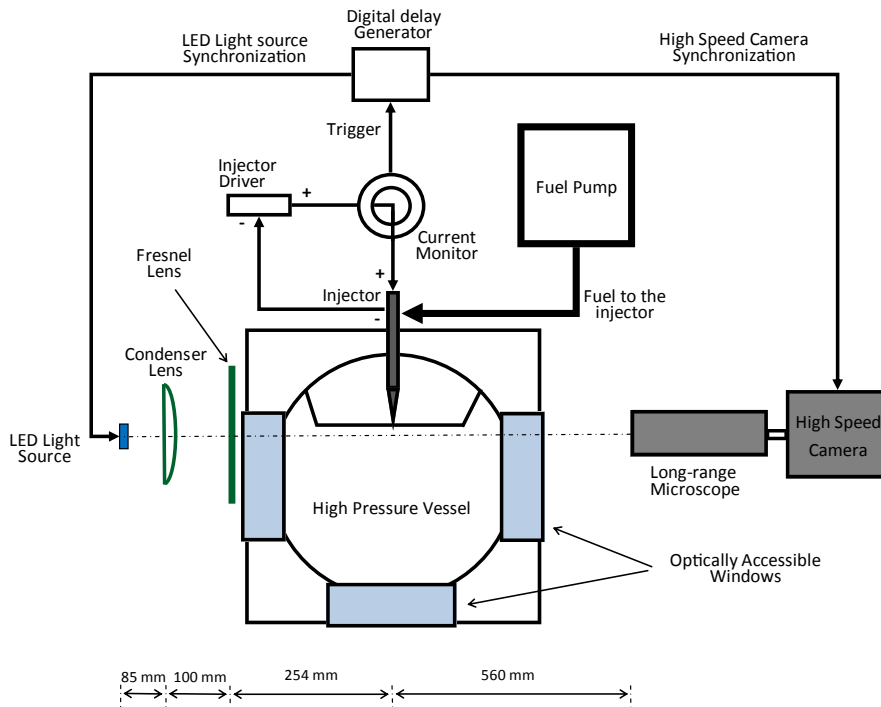


Figure 14: Complete experimental setup schematic

3.2 High Spatial and Temporal Imaging Tradeoffs

Even with state-of-the-art technologies for high-speed imaging, there are a number of trade-offs to consider in optimizing spatio-temporal resolution and image quality. These trade-offs require optimization of the optical system. This section outlines and explains the pertinent trade-offs that have been considered in the optical system design.

3.2.1 Illumination – Magnification Trade-off

The numerical aperture (NA) of a lens is a dimensionless number that specifies the range of angles over which light enters or exits the lens. The maximum half angle, θ , of the light collection cone (known as the acceptance cone) describes the maximum angle at which the lens can accept light rays from a particular point, as shown in Figure 15. This cone describes the light-gathering ability of the lens. Mathematically the numerical aperture (NA) is defined as:

$$NA = n \sin \theta \quad (1)$$

Where n is the refractive index of the space in which the source is located and θ is the one-half of the lens collection angle. The NA can also be expressed in terms of the lens $F/\#$ (ratio of focal length and diameter of the lens, f/D) as:

$$NA = \frac{1}{2F/\#} \quad (2)$$

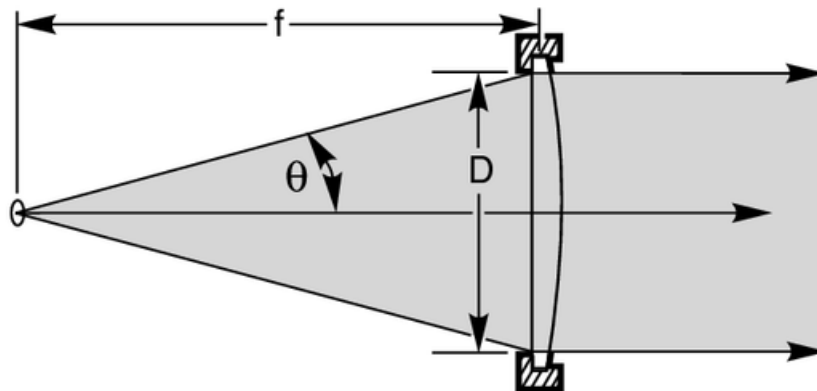


Figure 15: The Numerical Aperture and $F/\#$ of a lens [21]

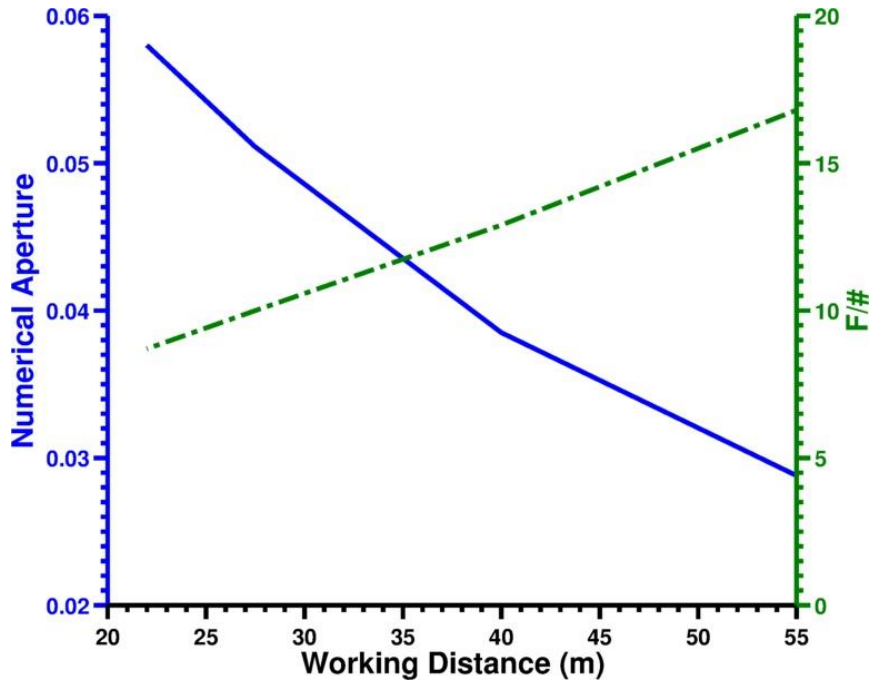


Figure 16: Questar QM1 Short-Mount Long-Range Microscope Numerical Aperture and F/# vs Working Distance

Figure 16 shows that NA increases with shorter working distances for the long-range microscope used in our imaging system (Questar QM1 Short-Mount Long Range Microscope). Thus, increasing the magnification of the optical system, by decreasing the distance between the lens and the object plane, increases its NA. This is of benefit for imaging objects at very high resolution since higher magnification, achieved by a shorter working distance, results in higher illumination at the image plane. However, there is a minimum working distance of 22 inches (~560 mm) for the long-range microscope used in the current work. Further increases in magnification require the addition of intermediate lenses between the long-range microscope and the camera sensor, which will expand the rays of light to over-fill the sensor. Part of the light is lost in the process as shown in Figure 17. The lower illuminance realized at the camera sensor will result in degraded image contrast and prevents imaging of the finer details of the spray.

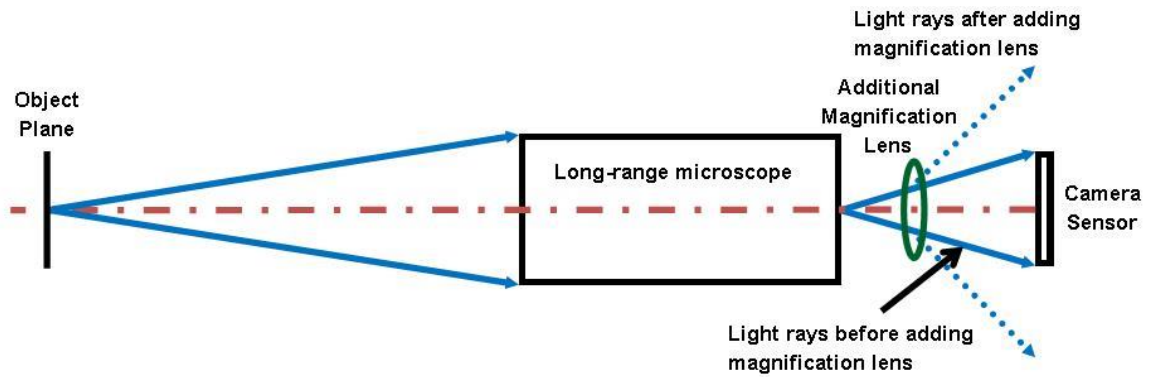


Figure 17: Effect of adding additional magnification lens to the long-range microscope

Figure 18 shows the illumination intensity measured by the camera sensor before and after adding the magnification lens. The images were taken with an LED pulse width of 90 ns. The illumination is measured in counts and with the 12-bit format of the SA-X2 sensor, the maximum intensity is 4096 counts. Magnification is measured by comparing the actual pixel size ($20\ \mu\text{m}/\text{pixel}$) to the measured image resolution in $\mu\text{m}/\text{pixel}$. It can be seen that the illumination intensity decreases by more than 7 times (from complete saturation at 4096 counts to 566 counts) as the magnification is increased from 2.46x to 12.6x. Thus, attempts to further increase image magnification using intermediate magnification lenses are accompanied by a significant degradation in image contrast

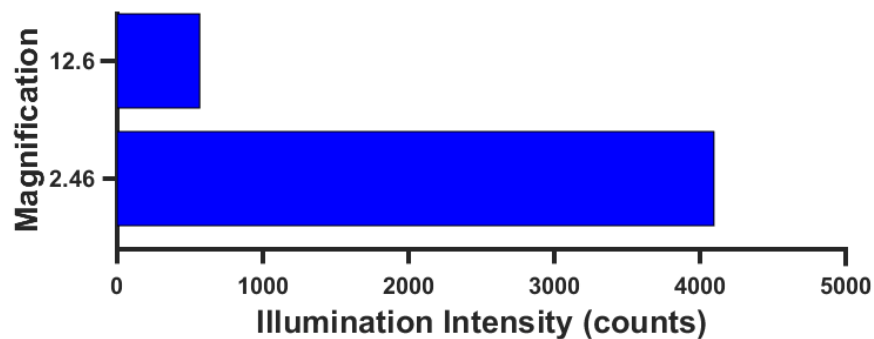


Figure 18: Reduction in illumination intensity with increasing magnification

3.2.2 Magnification – Field of view (FOV) Trade-off

The field of view of an image defines the dimensions of the image in physical units. As can be expected, increasing magnification of the optical system will result in a smaller field of view. Higher magnification reduces the spatial scale resolved by each pixel, which results in an overall reduction of FOV. To investigate the development of a feature of the spray (ligament or droplet) with time requires tracking that feature across successive frames. A larger FOV allows for that feature to remain in the image for a longer duration hence providing the opportunity to observe its temporal evolution for a longer period of time. Thus, increasing the magnification (and spatial resolution) of the optical system also compromises the ability to track the temporal evolution of a single spray feature. Figure 19 shows the ability of the employed optical system to resolve finer spray details with a higher magnification, and its effects on the FOV at framing rates of 200k and 480k. A higher magnification allows can resolve smaller objects in the image at the cost of a smaller FOV.

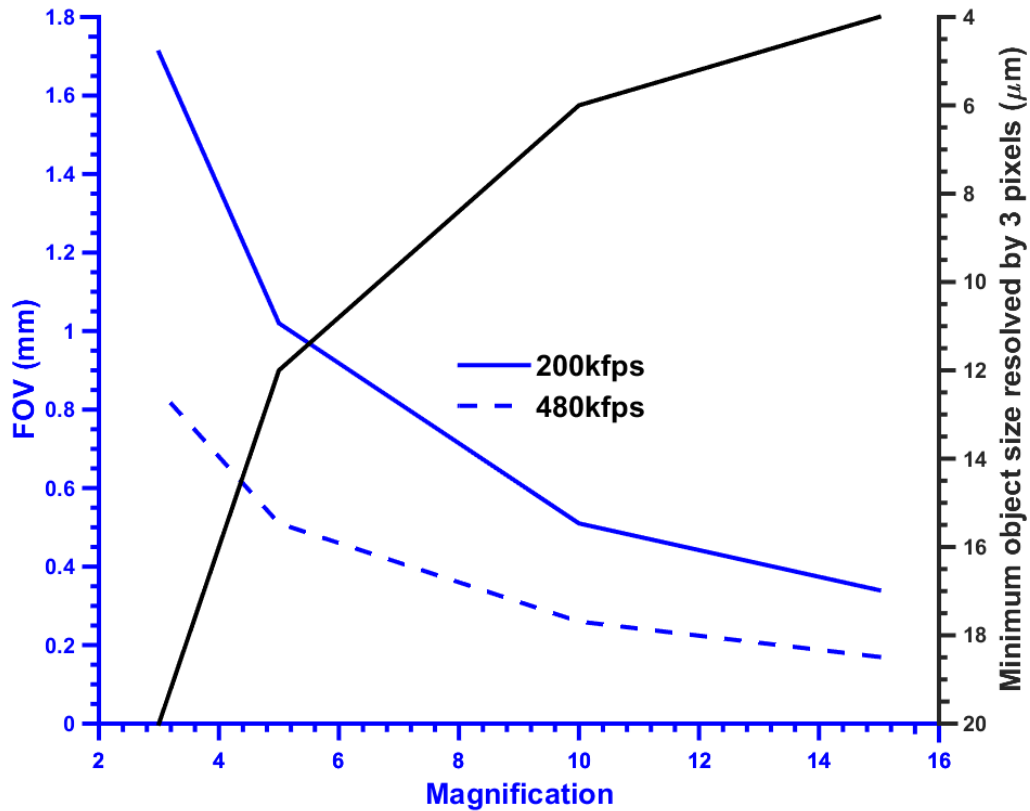


Figure 19: Reduction in FOV with increasing magnification

This effect of reduced FOV can also be viewed in terms of the maximum feature velocities that can be imaged using the optical system. A spray feature with velocity above a certain limit will leave the FOV before its development can be tracked. Figure 20 compares the maximum velocity with which a feature can travel in order to get three images of that feature before it leaves the frame. We see that this velocity decreases significantly at higher magnifications.

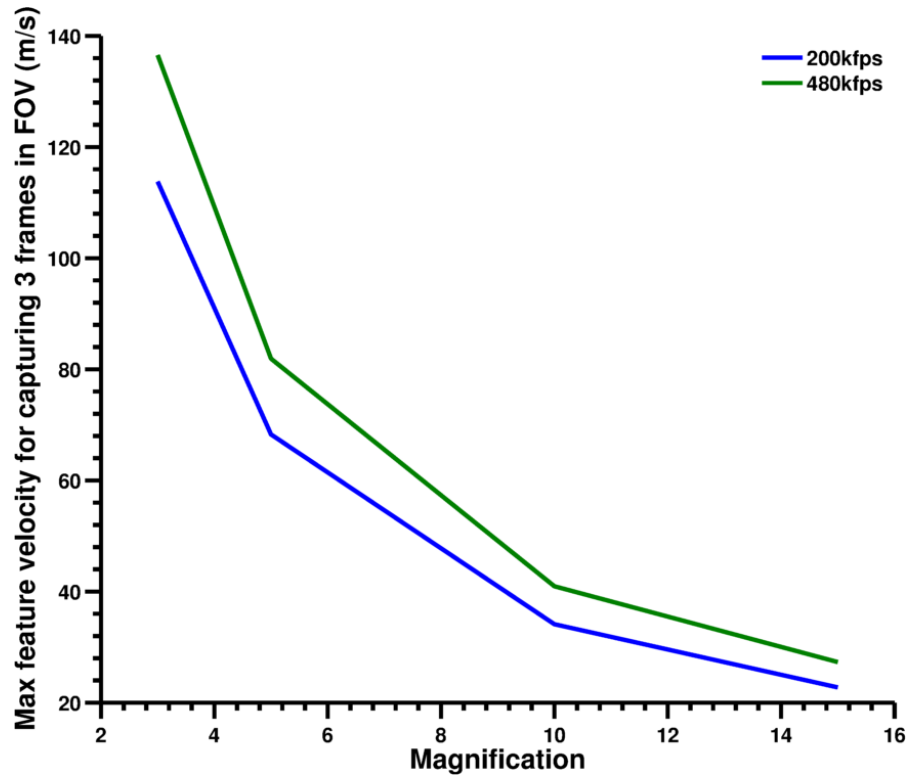


Figure 20: Reduction in maximum feature velocity for capturing 3 frames in FOV with increasing magnification

3.2.3 Framing rate – Field of view (FOV) Trade-off

Figure 19 also shows that the employed framing rate will affect the image FOV. Current technologies in high-speed imaging limit the number of active pixels in the camera sensor at high framing rates. This limitation is due to the fact that the previous image on sensor needs to be transferred to the memory and flashed from the sensor before it is ready to take the next image. It becomes exceedingly difficult to perform this process at higher framing rates and is managed by reducing the number of pixels to be flashed. As the FOV is dependent on the number of active pixels, imaging at higher frame rates reduces the FOV, which has the same effect as explained above. Figure 21 shows the reduction in the FOV (in pixels) with increasing frame rates for the Photron

Fastcam SA-X2 High-Speed camera. The active pixels reduce from 1 megapixels (1024 x 1024) at 1000 frames per second to 6144 pixels (128 x 48) at 480,000 frames per second.

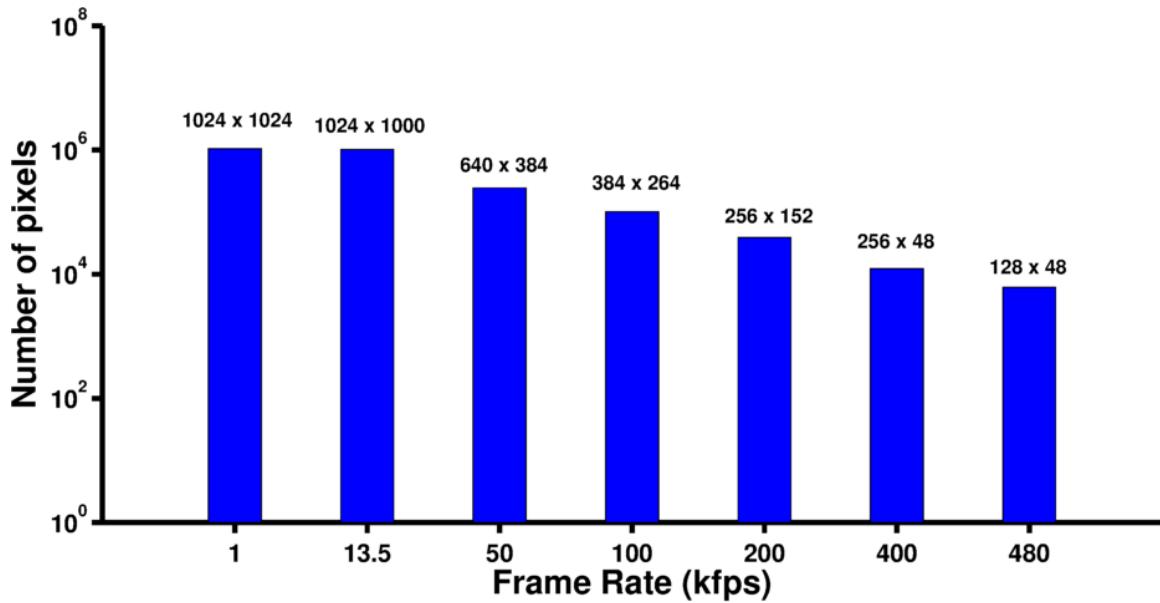


Figure 21: Reduction in FOV with increasing frame rate (the data labels show dimension of FOV in pixels)

3.2.4 Light pulse width – Illumination Trade-off

As explained earlier, high pressure fuel sprays require very high spatial and temporal resolutions to image and track the features formed at the interface. Another imaging system requirement is the need to freeze the motion of these features in each frame to avoid blur. A feature will become blurred if it moves more than the length of a single pixel within the exposure time. Figure 22 shows the maximum possible exposure time allowed, above which blurring will occur, for increasing feature velocities at different imaging resolutions. A theoretical spray velocity has also been plotted for iso-octane at room temperature and pressure with increasing injection pressures. This figure reveals the crux of imaging high-pressure fuel sprays. Assuming that the features move

with mean Bernoulli velocity of the injected liquid, we see that for a $1\mu\text{m}/\text{pixel}$ resolution, even an exposure time as short as 10 ns is not fast enough to fully freeze the feature within a pixel. Although these are ideal velocities and real feature velocities will definitely be slower, this figure shows that imaging at sub-micron pixel resolution requires exposure times faster than 10 ns, even for injection pressures as low as 5 MPa. Hence, imaging high-pressure diesel sprays (operation pressures ~ 500 MPa) at sub-micron resolution is virtually impossible with current technologies. For this reason, the current work has focused on GDI sprays that operate at 10-60 MPa injection pressures and offer a better opportunity freeze the spray motion at high spatial resolutions.

Even with this consideration, an exposure of the order of 100 ns is not possible using the camera shutter. The Photron Fastcam SA-X2 offers a fastest shutter of $1\mu\text{s}$, which is at least an order of magnitude more than the desired exposure times. This problem is dealt with using pulsed LEDs as optical shutters. In the current system, the LightSpeed LED can be pulsed as fast as 20 ns. However, the problem with using such short exposure times is the amount of illumination that can be obtained in the image. With the pulsed LED illumination system, even a $5\mu\text{s}$ long camera exposure will only receive light for the duration of the LED pulse (min 20 ns), which reduces the image illumination. High-powered LEDs are ideal in this situation because they have the capability to be overdriven when being pulsed and can deliver 10-15 times more power in a short pulse as compared to the power they deliver in continuous mode. Within pulsed mode, increasing the pulse width of the LED will provide better illumination (longer light integration times), but at the expense of blurring the spray features. Hence a compromise has to be made between the requirements for illumination (contrast) and the minimum

pulse width of the LED to resolve high-velocity features. The comparison between different pixel resolutions is to show the effect of magnification on exposure durations. As the magnification increases, the pixel resolution decreases, which requires shorter pulse widths to avoid blur.

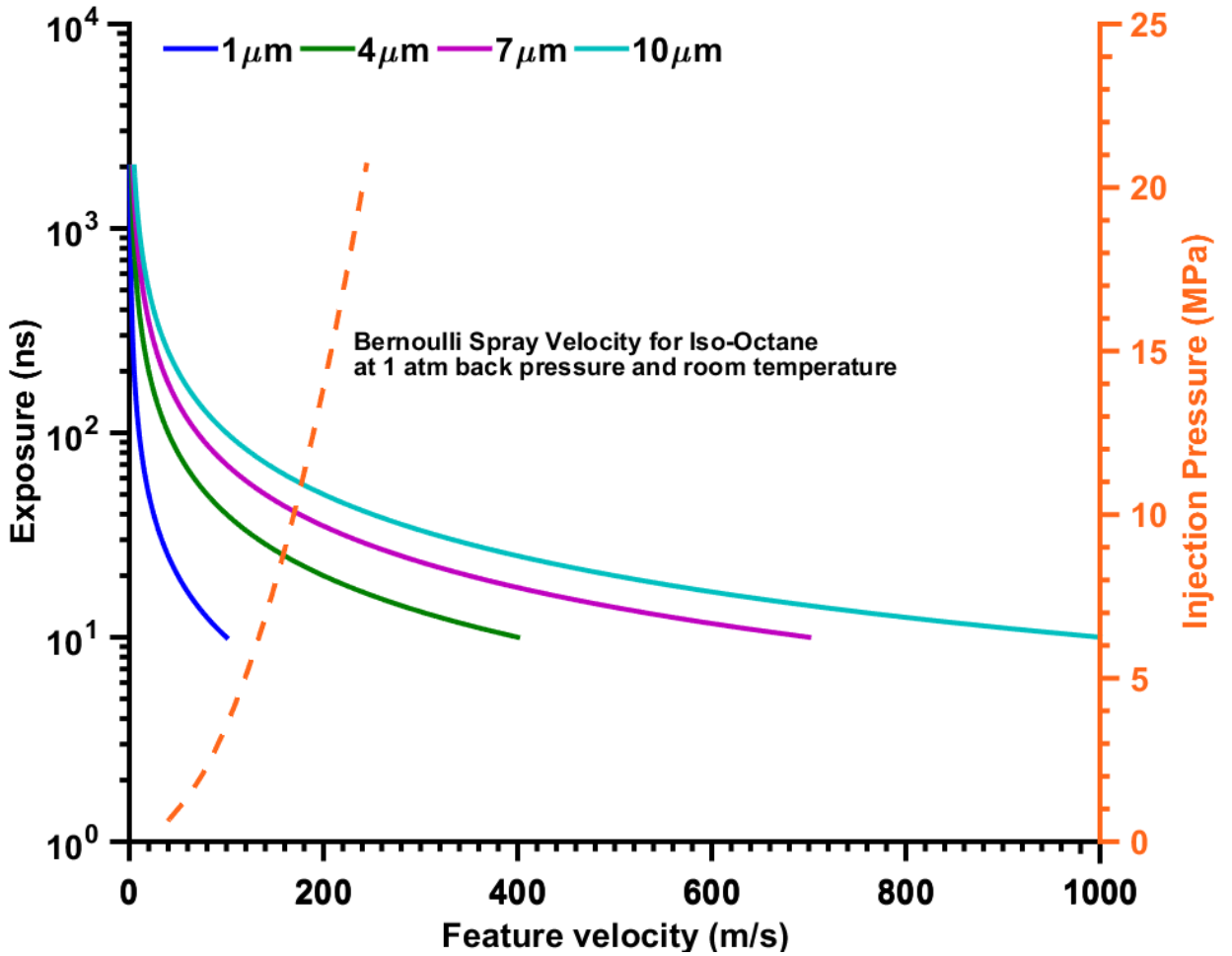


Figure 22: Maximum feature velocity for a given exposure duration to avoid blur

3.3 Illumination system setup

The ideal design of the illumination system would result in collection of all the light emitted from the light-source at the image sensor (maximum throughput). This is the ideal case and the setup we designed was based on emulating the ideal case as closely as

possible. The physical constraints in the design of the system are: (i) the finite size of the LED light source of 1 mm x 1 mm; (ii) the 50-cm distance from window to window in the high pressure vessel, between which no optical equipment can be placed; (iii) the 56-cm minimum working distance of the long-range microscope, which is the minimum distance from the imaging plane (spray tip) to the lens of the long-range microscope; and (iv) the size of the image FOV, which is 1.77 mm x 1.06 mm for a 2.9x magnification and 0.37 mm x 0.22 mm for a 13.7x magnification at 200 kfps (the calculation for magnification and the size of the FOV will be shown later). In order to account for the approximations and achieve a uniform illumination for the entire FOV, the illumination spot size at the object plane was fixed to a conservative value of 3 mm.

Figure 23 shows the viewing cone or collection angle for the long-range microscope at a working distance of 560 mm. The principle for the design of the illumination system is to collect as much light as possible from the source and focus it at the tip of this cone, which means that the f/no of the condensing lens at the light source should be as small as possible and the spot size of the light at the tip of the cone should be the size of the FOV. This enables the long-range microscope to view the highest illuminance at the object plane.

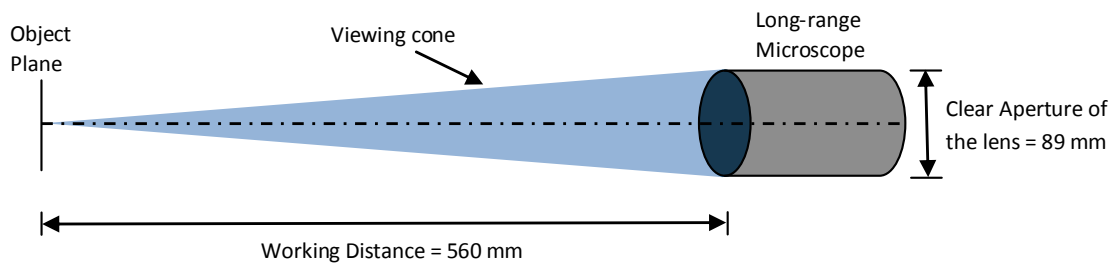


Figure 23: Viewing cone of the Questar QM1 short mount long-range microscope

The focal length and diameter of the lenses required to achieve an illumination spot size of 3 mm were calculated using the concept of the optical invariant. The optical invariant is a fundamental law of optics which states that in any optical system comprising of only lenses, the product of the image or object size and ray angle is constant, or invariant, of the system. For a single lens, the optical invariance can be proved using the ray diagram as shown in Figure 24. Choosing the maximal ray, which is the ray that makes the maximum angle with the optical axis as it leaves the object and passes through the lens at its maximum clear aperture, we have for small angles (using the paraxial approximation assumption)

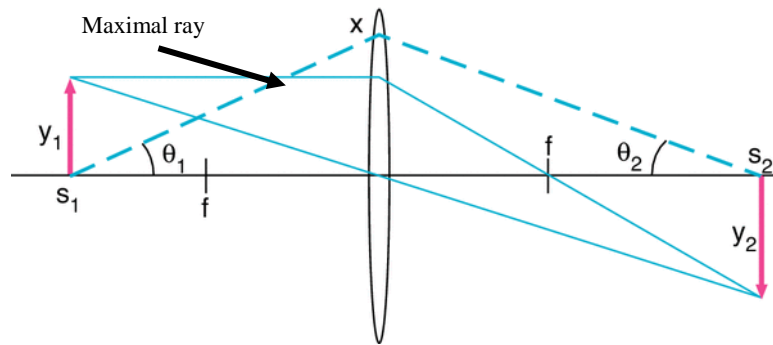


Figure 24: Optical ray trace for a single lens showing the maximal ray [22]

$$\theta_1 = \frac{x}{s_1} \text{ and } \theta_2 = \frac{x}{s_2} \quad (3)$$

And from the basic definition of magnification

$$M = \frac{s_2}{s_1} = \frac{y_2}{y_1} \quad (4)$$

Combining equation (3) and (4) yields the proof of the optical invariance as shown in equation (5)

$$y_1\theta_1 = y_2\theta_2 \quad (5)$$

This result is valid for any ray traced from an object to the image and is also valid for any number of lenses, as could be verified by tracing the ray through a series of lenses [22].

Our illumination system design required the use of two lenses because the physical constraints of the system made it impossible to collect the maximum amount of light from the source and focus it to a spot the size of FOV at the imaging plane. A schematic of the two-lens system is shown in Figure 25. The first lens is called the condenser lens and the second lens is called the focusing lens. With the light source at its focus, the condenser approximately collimates the light which is then refocused on the imaging plane by the focusing lens. Because of the finite extent of real light sources, the light can only ever be approximately collimated, and the magnitude of divergence is governed by the size of the source and the focal length of the condenser lens. From Figure 25, the optical invariant for the two-lens system can be expressed as follows (assuming small angles)

$$h_2f_1 = h_1f_2 \quad (6)$$

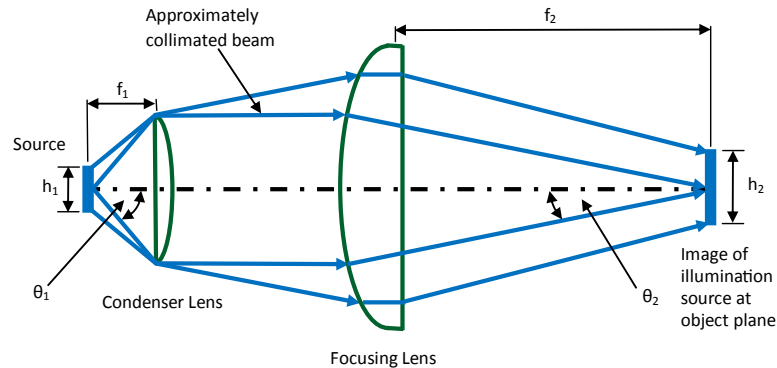


Figure 25: Schematic for the two lens system for the illumination setup

The physical constraints of our system define three of the four parameters in equation (6) as:

$$h_1 = \text{size of the LED source} = 1 \text{ mm}$$

$$h_2 = \text{spot size at the imaging plane (FOV)} = 3 \text{ mm}$$

$$f_2 = \text{Distance from the optical window to the imaging plane} = 250 \text{ mm}$$

Using the above parameters we calculated the required focal length of the condenser lens to be 83.33 mm.

The next step was the selection of a condenser lens and focusing lens from a list of commercially available lenses having a focal length close to 83.33 mm and 250 mm respectively. Another requirement for the condenser lens was to have a small f/no to collect the maximum light from the source. A Fresnel lens with a focal length of 254 mm (10 in) was selected as the focusing lens. With the focusing lens selected ($f_2 = 254$ mm), the spot size, h_2 , was recalculated for a selection of condenser lenses which had a focal length close to 83.33 mm. Table 1 shows the list of available lens options and their respective f-numbers.

Figure 26 shows the product of the spot size and f/no, as an indication of the light throughput of the lens system, for each of these lenses. Lens 2 was selected since it has the minimum product, which indicates that it provides the best combination of light collection at the illumination source (low f/#) and high illuminance at the object plane (small spot area). The final schematic of our illumination system is shown Figure 27.

Table 1: Lens options for the design of the illumination system

| # | Lens | f/no |
|---|--|------|
| 1 | Aspheric lens, $f=60$ mm and $D = 75$ mm | 0.8 |
| 2 | Plano-Convex lens, $f = 85$ mm and $D = 75$ mm | 1.13 |
| 3 | Aspheric lens, $f = 59$ mm and $D = 80$ mm | 0.74 |
| 4 | Plano-Convex lens, $f = 75$ mm and $D = 75$ mm | 1.00 |
| 5 | Plano-Convex lens, $f = 88.3$ mm and $D = 50.8$ mm | 1.74 |
| 6 | Plano-Convex lens, $f = 100$ mm and $D = 50.8$ mm | 1.97 |

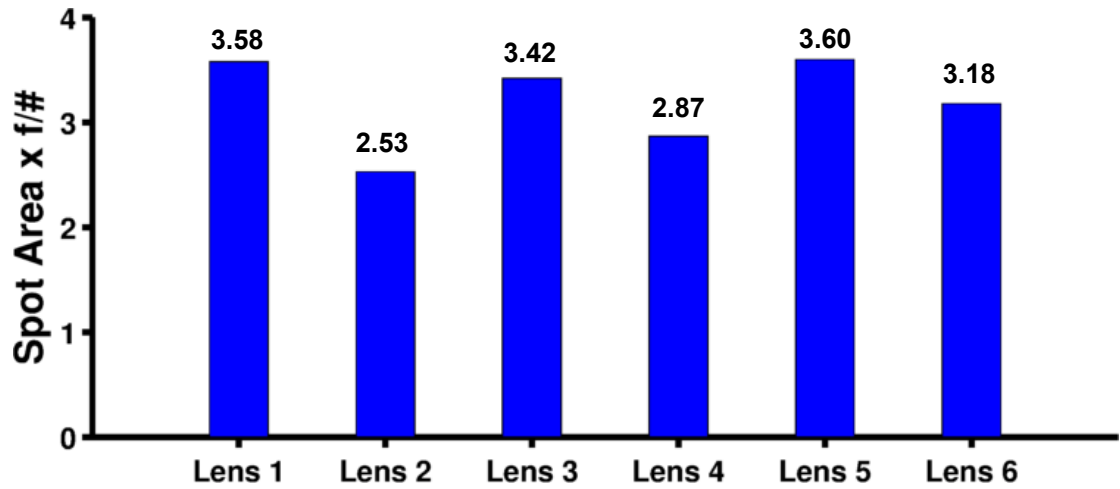


Figure 26: The product of spot size and f/# for the lens choices listed in Table 1

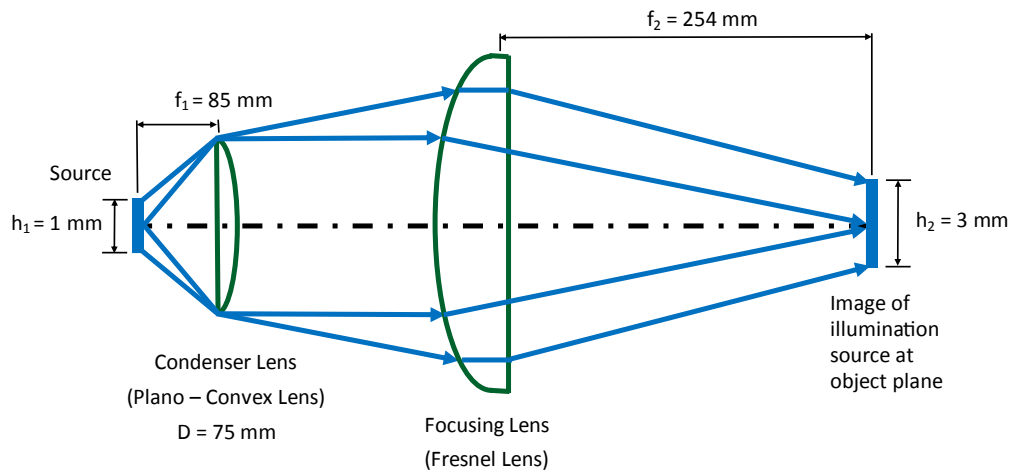


Figure 27: Final schematic of the illuminating system with focal lengths and diameters of the lenses and the size of the source and image

3.3.1 Optical power at the imaging plane

With the illuminating system setup designed, the optical power was measured at the imaging plane to quantify how the peak optical power varied with varying pulse width. A switchable gain photodiode (Thorlabs PDA36A) was used to measure the optical power because its bandwidth of 10 MHz was capable of registering the short (20 - 90 ns) pulses from the LED.

Figure 28 shows the resulting measured optical power with increasing LED pulse width. The trend is not quite linear and shows a decreasing peak optical power for shorter illumination pulse widths. A longer pulse width gives more optical power but also causes a greater thermal loading on the LED. This higher thermal load on the LED, when operated at longer pulse widths, causes it to dim after a certain number of pulses.

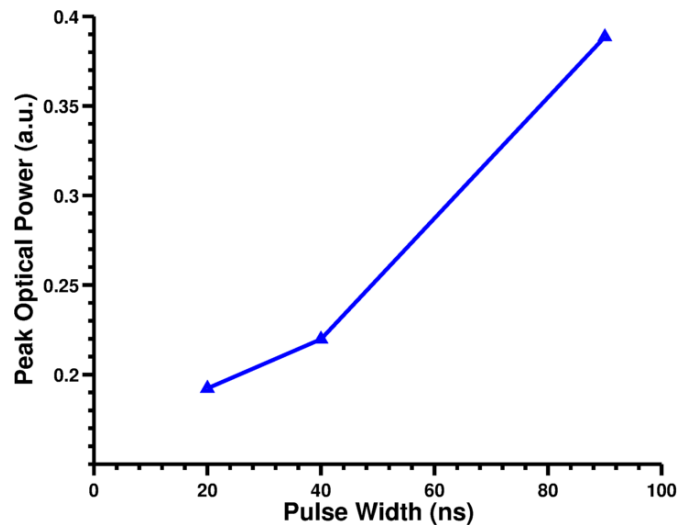


Figure 28: Optical power measured at the spray plane by PDA36A – Si Switchable Gain Detector

3.3.2 Image resolution quantification

The resolution and performance of the imaging system can be characterized by a quantity known as the modulation transfer function (MTF). The MTF measures the

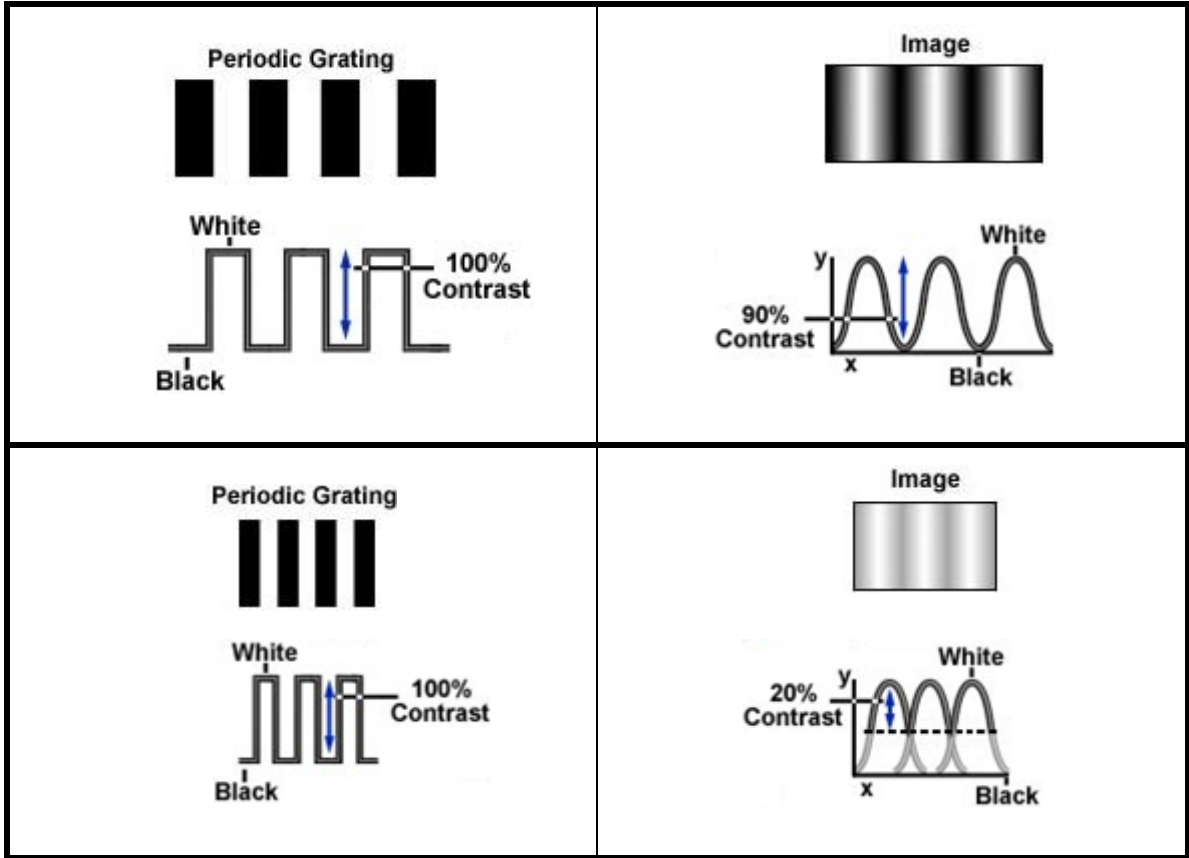
ability of a lens to transfer contrast from the object to the image. It can also be explained as the measure of how faithfully the lens reproduces or transfers detail from the object to the image. Computation of the modulation transfer function is a means to incorporate resolution and contrast data of the imaging system into a single specification. One of the experimental methods of calculating MTF is to image a target with high contrast periodic grating of varying spatial frequencies. An example of the high contrast periodic grating with varying spatial frequencies is shown in Figure 29(a). When this object is imaged it produces an image as shown in Figure 29(b), in which the clarity of the edges deteriorates progressively for smaller spatial scales in the image. The blur effect is due to diffraction and imperfections of the lens. Diffraction causes the light to bend as it passes through the narrow passages between the gratings which results in a decrease of contrast and blur in the image. As the gratings become progressively closer, the effect of diffraction is more pronounced and results in a greater modulation of contrast from the object to the image until the image is completely grey and no modulation can be observed at all. The imperfections in a lens amplify the effect of diffraction and cause a greater modulation of contrast. Diffraction is the fundamental optical limit on image quality and resolution that results from the wave nature of light and the finite diameter of the lens. A perfect imaging system is called diffraction-limited because the only thing that is limiting its performance is diffraction.



Figure 29: (a) High contrast periodic grating and (b) Image of the high contrast periodic grating

Figure 30 shows a schematic picture of the contrast transfer from object to image for a low and a high spatial frequency periodic grating. It can be seen from the figure that

the low frequency grating has a 90% contrast transfer whereas the high frequency grating results in only 20%.



(a)

(b)

Figure 30: (a) Periodic gratings with their contrast (b) Images of these periodic gratings with their contrast

From the figure, the image contrast or modulation can be defined as

$$\text{Image Modulation } (M) = \frac{(I_{max} - I_{min})}{(I_{max} + I_{min})} \quad (7)$$

Where I_{max} and I_{min} are the maximum and minimum contrast in the image respectively.

And the modulation transfer function can then be calculated as

$$MTF = \frac{\text{Image Modulation}}{\text{Object Modulation}} \quad (8)$$

Where the objection modulation for a test target is always 1.

To quantify the MTF of the current imaging system, a 1951 USAF resolution test target, as shown in Figure 31, was imaged. This target has a series of horizontal and vertical lines which are used to determine the resolution of an imaging system. The target consists of ten groups, each with six elements, and has spatial frequencies in the range of 0.250 lines/mm to 228 lines/mm.

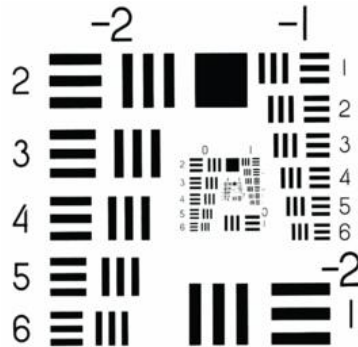


Figure 31: 1951 USAF test target for MTF calculation

The MTF of the designed imaging system is shown in Figure 32. Since the MTF is dependent on the illumination as well as the collection system, the plot is shown for two illuminating pulses widths (20 and 90 ns), which have been used for spray imaging at 2.9X magnification and at 13.7x magnification, respectively. Only a 90-ns pulse is used for higher magnification because it is the minimum pulse width that produced sufficient illumination to visualize the spray at this magnification. From the figure it can be seen that the MTF of the image produced with a 20-ns illumination pulse is slightly better than the 90-ns pulse. This occurs because the image is saturated at the 90-ns pulse width, which causes charge bleeding to neighboring pixels on the sensor, resulting in a lower image contrast. Hence, preventing saturation in the image helps to enhance contrast transfer. Figure 32 also shows that the low magnification case of 2.9x can only transfer contrast for spatial frequencies of up to 72 lines/mm, whereas the higher magnification case of 13.7x can transfer contrast at spatial frequencies of 102 lines/mm. The lower spatial frequencies cannot be plotted for the 13.7x case because of the reduced FOV.

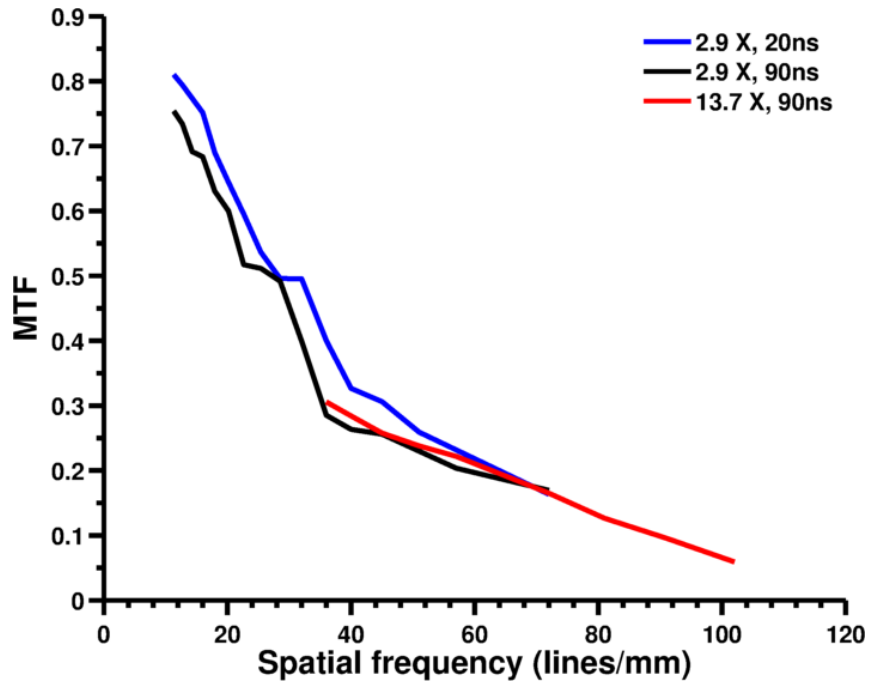


Figure 32: Modulation Transfer Function of the designed optical system

The magnification values quoted above and the size of FOV is also calculated from the test target image. The resolution of each pixel is calculated from the known spatial frequencies in the target, from which we can calculate the magnification using the actual size of the pixel in the camera sensor of 20 μm . The FOV can also be calculated using the pixel size and the number of active pixels. These values are summarized in Table 2.

Table 2: Pixel Size, magnification and size of FOV for 200 kfps and 480 kfps framing rate

| Pixel Resolution (μm) | Magnification | Number of active pixels for 200 kfps | FOV for 200 kfps (mm x mm) | Number of active pixels for 480 kfps | FOV for 480 kfps (mm x mm) |
|------------------------------------|---------------|--------------------------------------|----------------------------|--------------------------------------|----------------------------|
| 6.94 | 2.9x | 256 x 152 | 1.77 x 1.06 | 128 x 48 | 0.89 x 0.33 |
| 1.46 | 13.7x | 256 x 152 | 0.37 x 0.22 | 128 x 48 | 0.19 x 0.07 |

CHAPTER 4: RESULTS AND DISCUSSION

All tests for the high-speed imaging of the GDI spray were performed in non-evaporating conditions. The ambient pressure for the tests was varied from atmospheric pressure to 10 bar (1 MPa). Figure 33 shows the shadowgraph of the whole spray (all five individual jets from the five holes) at atmospheric temperature and pressure and ~ 200 bar (3000 psi) injection pressure. The injector is oriented such that the spray from the four angled holes are pointing upwards and their respective jets are thus moving in the upward directions whereas the axial jet is aligned with the horizontal. This makes the horizontal spray ideal for near-nozzle microscopy since its interface is not obstructed by other jets and can be viewed clearly. The area under observation by the near-nozzle microscopy is shown in red box.

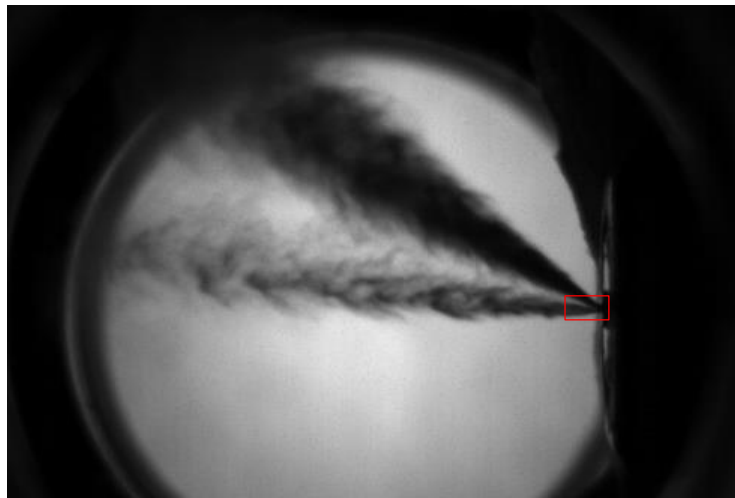


Figure 33: Shadowgraph of the whole spray at atmospheric temperature and pressure and 3000 psi injection pressure

Initial microscopy of the spray was performed at injection pressures of 3000 psi (200 bar). Figure 34 shows a sequence of 6 images taken at 2.9x magnification at a framing rate of 200 kfps and an exposure of 90 ns. Since we are studying the steady state behavior of the spray, the time stamps shown on the top left corner are relative to the first image. The spray is moving from right to left in the images. Interfacial instabilities can be seen to form on the lower interface of the spray with droplets visible further downstream. Since these images are taken at 200kfps the separation between each frame is 5 μ s. This time duration restricts tracking the development of the ligament through successive frames so it is not possible to develop a link between the ligament and the droplet formation. The interface of the spray also appears rather blurred, which could occur due to a number of reasons, including (i) defocused objects beyond the depth of field of the lens (ii) clusters of small features below the resolving power at this magnification (iii) features moving very fast, which cannot be frozen in the frames with a 90 ns exposure.

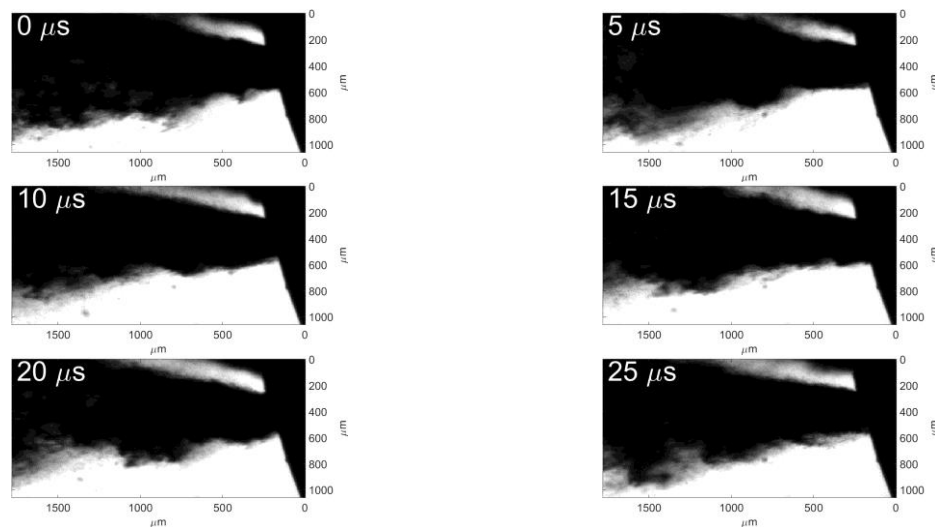


Figure 34: Microscopic images of the spray at 21 MPa (3000 psi) injection pressure. 2.9x magnification, 200 kfps framing rate and 90 ns exposure.

Increasing the magnification enables us to assess the issue of the size of features. Figure 35 shows a sequence of 6 images of the same spray taken at 13.7x magnification at the same framing rate of 200 kfps and an exposure of 90 ns. Since these images are at a higher magnification, the illumination of these images was reduced, as explained earlier in the high-speed imaging tradeoff section. Hence the images have been processed to enhance contrast by 20 %. The blurred interface is again visible in these images which shows that the blurriness is most likely not because of the smaller size of the features. The tracking of features is again not possible in the 13.7x magnification images because the speed of the spray is the same and the FOV has been reduced significantly which causes the feature to move out of the FOV within the time between frames.

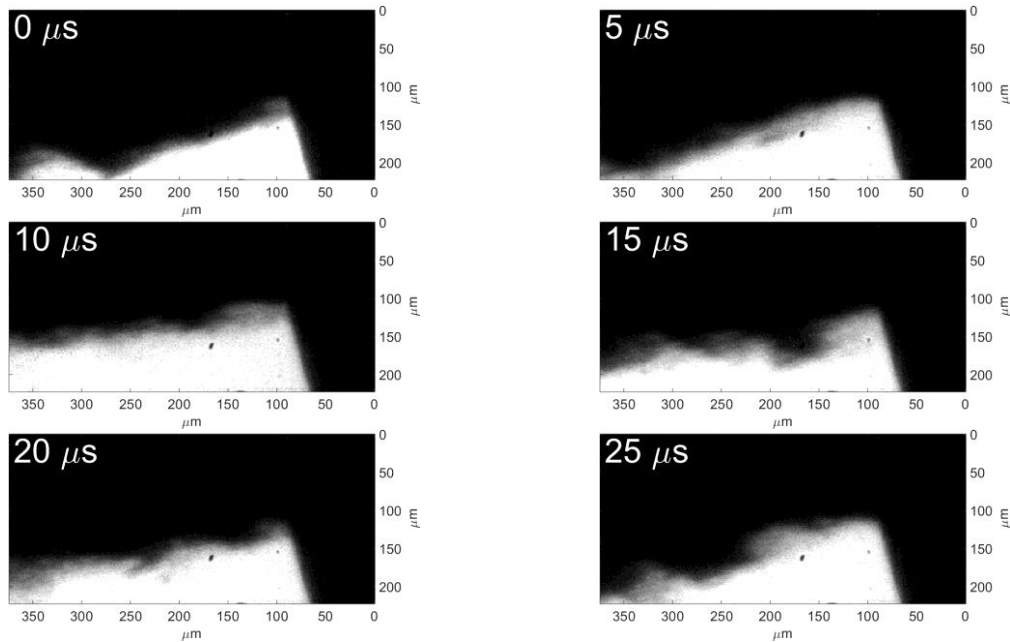


Figure 35: Microscopic images of the spray at 21 MPa (3000 psi) injection pressure. 13.7x magnification, 200 kfps framing rate and 90 ns exposure.

Figure 36 shows the 3000 psi spray at a higher framing rate of 480 kfps at 2.9x magnification and a 20 ns exposure. The exposure is reduced due to the maximum duty cycle of 1% for the Light-Speed LED which restricts the maximum pulse width to 20 ns

for a pulse repetition rate synced to the camera framing rate of 480 kfps. Higher magnification images are not possible at 480 kfps framing rate because the 20 ns exposure does not provide sufficient illumination at that magnification. Because of reduced illumination due to lower exposures the images are processed to increase contrast by 30%. Since each successive frame is only 2.1 μs apart, the development of the features can now be tracked. It can be seen from Figure 36 that the feature that is formed in the middle of the image at 4.2 μs moves to the left in the next frame and also grows in size. Similarly the feature that develops in the 8.4 μs frame grows and moves to the left in the 10.5 μs frame. The blurriness at the interface has also been reduced because of the 20 ns exposure but it has not been eliminated completely.

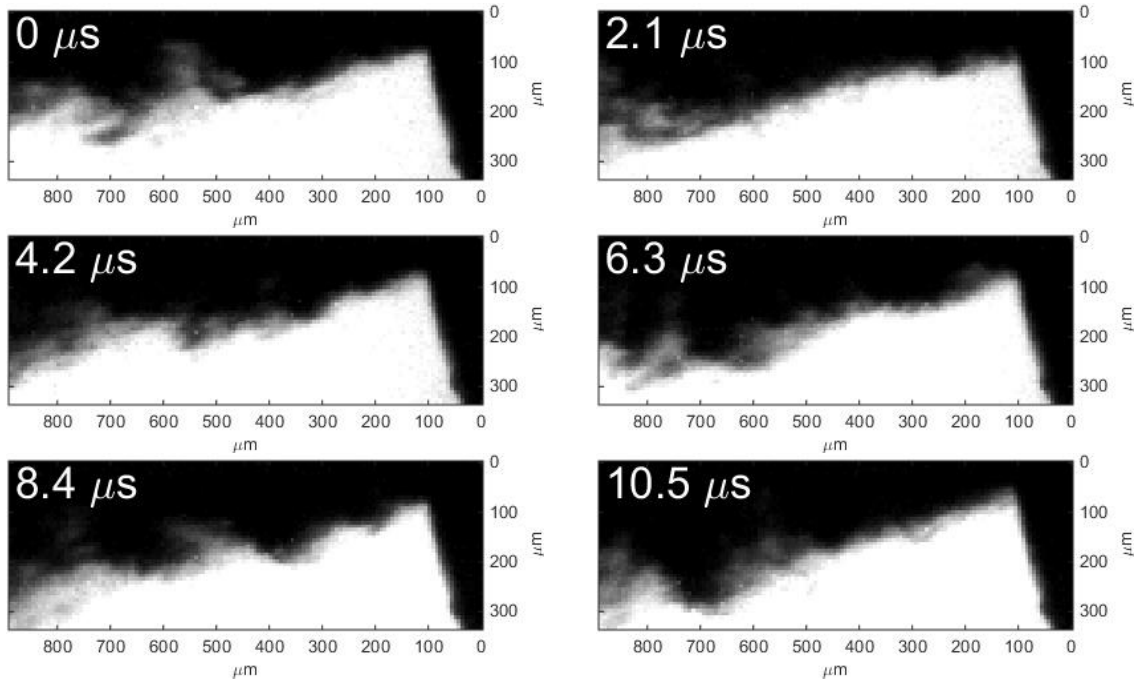


Figure 36: Microscopic images of the spray at 21 MPa (3000 psi) injection pressure, 2.9x Magnification, 480 kfps framing rate and 20 ns exposure.

The injection pressure of the spray was then decreased to be able to observe the interface and droplet formation with greater detail. Reducing the injection pressure results in a slower spray, which enabled us to freeze it in the frame with a 90 ns exposure. The injection pressure was initially decreased to an intermediate pressure of 1000 psi (80 bar). Figure 37 shows the images of the 1000 psi spray imaged at 2.9x magnification whereas Figure 38 shows the 1000 psi spray imaged at 13.7x magnification. It can be seen from the low magnification images that the interfacial instabilities are more clearly visible and the blurred effect is reduced but it is still difficult to track features across the frames.

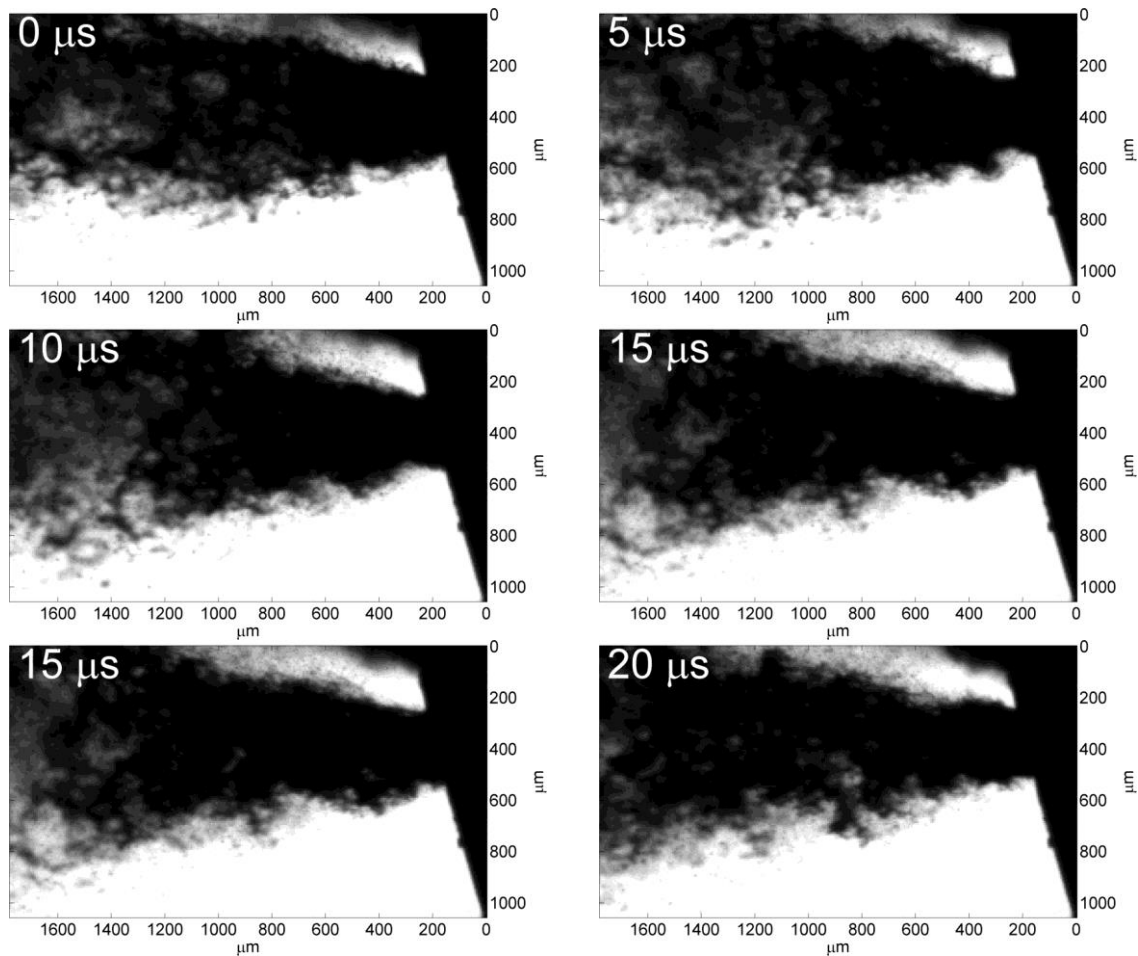


Figure 37: Microscopic images of the spray at 6.9 MPa (1000 psi) injection pressure, 2.9x Magnification, 200 kfps framing rate and 90 ns exposure.

The high magnification images in Figure 38 shows the interfacial instabilities in more detail and we can observe the development of these instabilities in successive frames for example the ligament that is visible in the 10 μs frame has grown and moved further downstream in the next frame. In addition to that we can also see in the 20 μs and the 25 μs frames how the finer ligaments are separating from the spray and forming droplets.

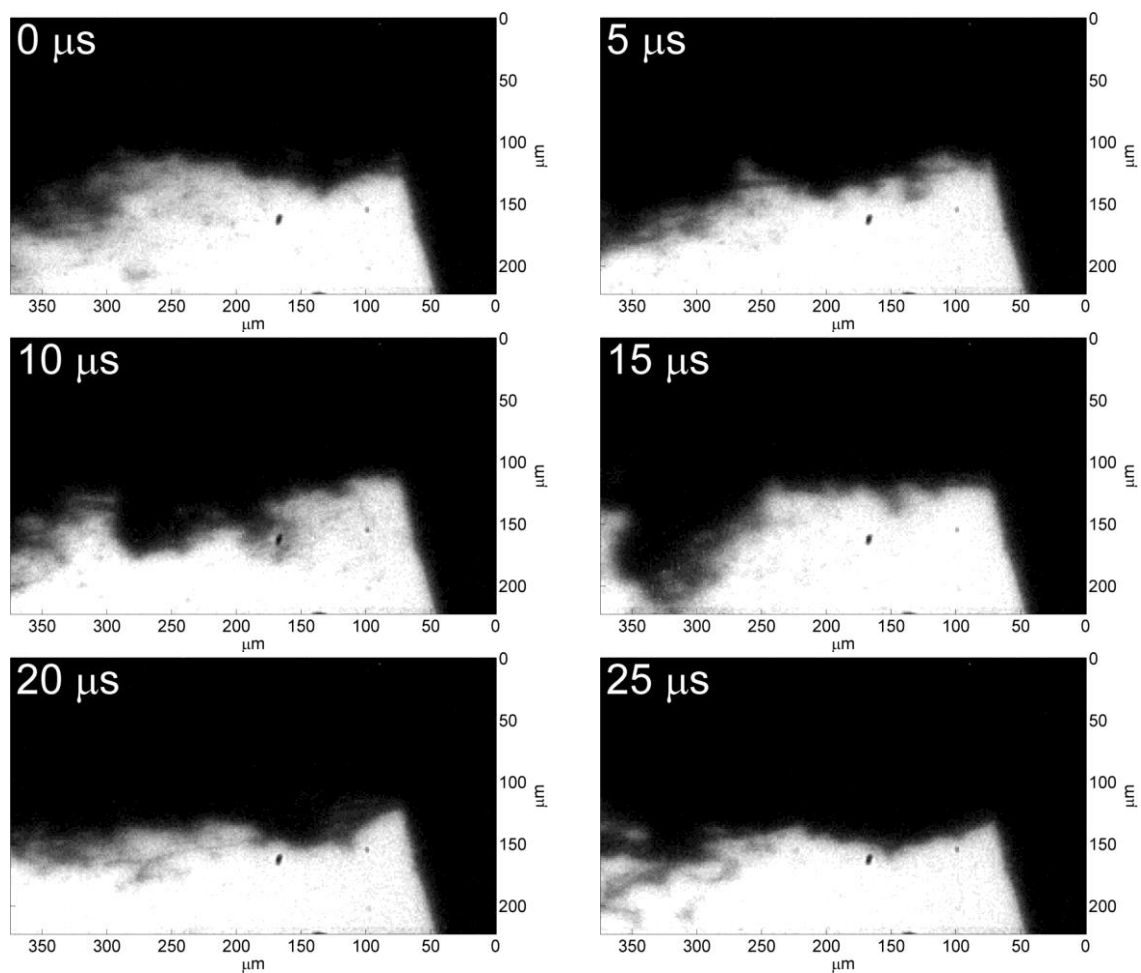


Figure 38: Microscopic images of the spray at 6.9 MPa (1000 psi) injection pressure, 13.7x Magnification, 200 kfps framing rate and 90 ns exposure.

Figure 39 shows the same 1000 psi spray imaged at a 480 kfps framing rate and 2.9x magnification and 20 ns exposure. The higher temporal resolution allows to follow the ligaments as they move downstream in successive frames. We can clearly see them forming in the first frame at 0 μs and then growing and moving downstream in the following frames. The separation of the finer ligaments from the main spray to form droplets can also be seen in the figure.

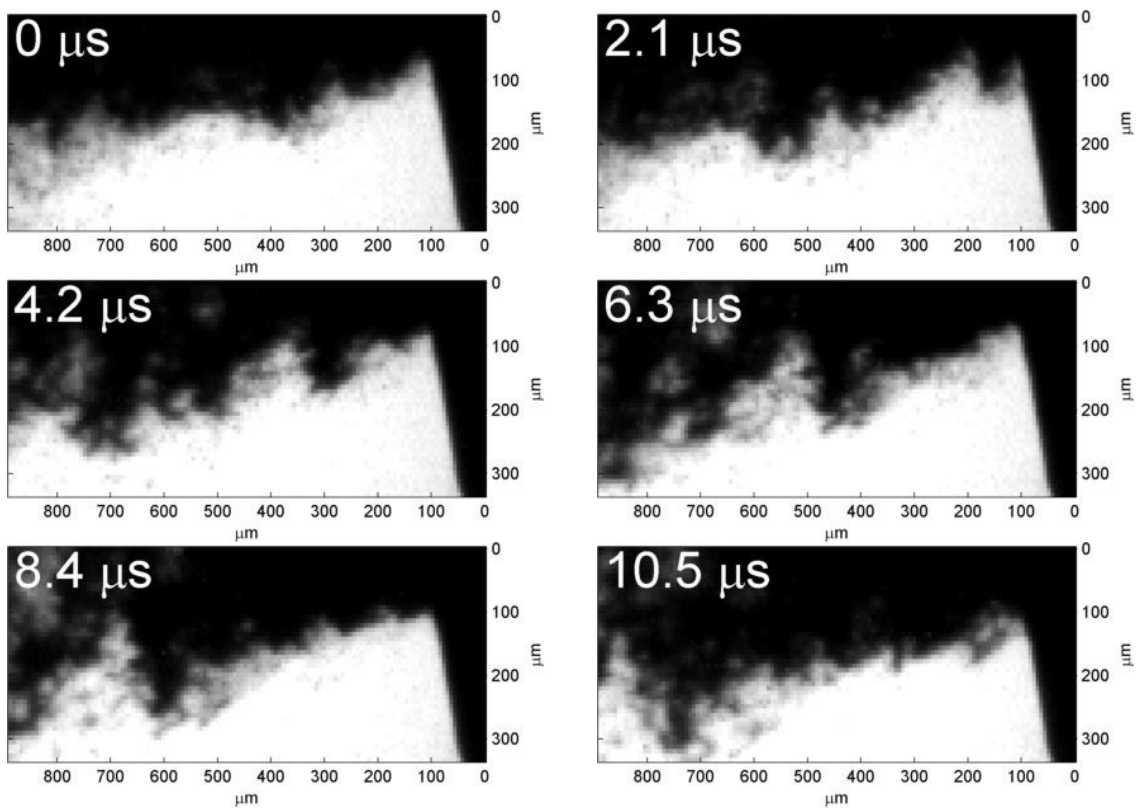


Figure 39: Microscopic images of the spray at 6.9 MPa (1000 psi) injection pressure, 2.9x Magnification, 480 kfps framing rate and 20 ns exposure.

The injection pressure of the spray was further decreased to be able to observe the interface and droplet formation in even more detail. Figure 40 shows the spray at 200 psi injection pressure imaged with 2.9x magnification at 200kfps framing rate and 90 ns exposure. It can be seen that there is no blurring in these images near the nozzle exit and

the formation of the ligaments and their successive separation into droplets is vividly visible. This is because the ligaments formed at this reduced injection pressure are larger in size and moving slower than the high pressure sprays which significantly improves the quality of the images in Figure 40.

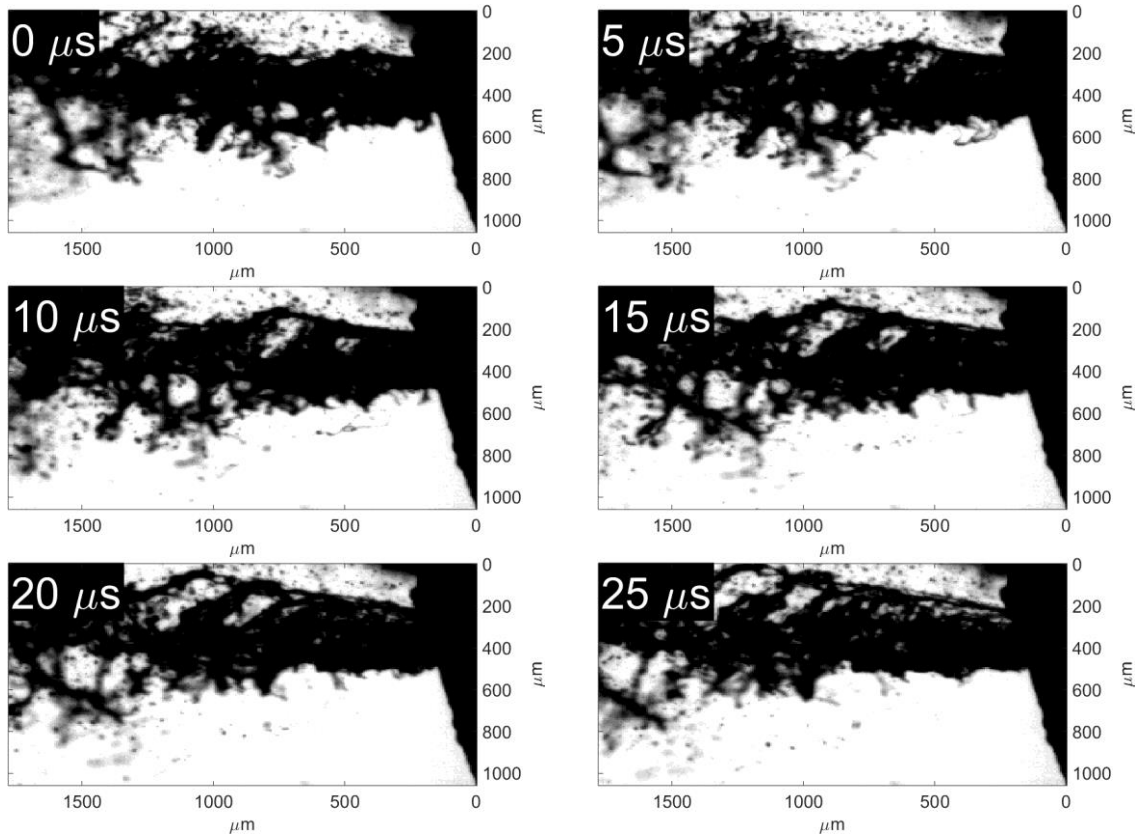


Figure 40: Microscopic images of the spray at 1.4 MPa (200 psi) injection pressure, 2.9x Magnification, 200 kfps framing rate and 90 ns exposure.

Higher magnification images of the same spray at 200 kfps and 90 ns exposure are shown in Figure 41. It can be seen from the figure that the interface of the spray is well defined and there is no blur in the image. The formation and propagation of ligaments can be tracked easily in these images.

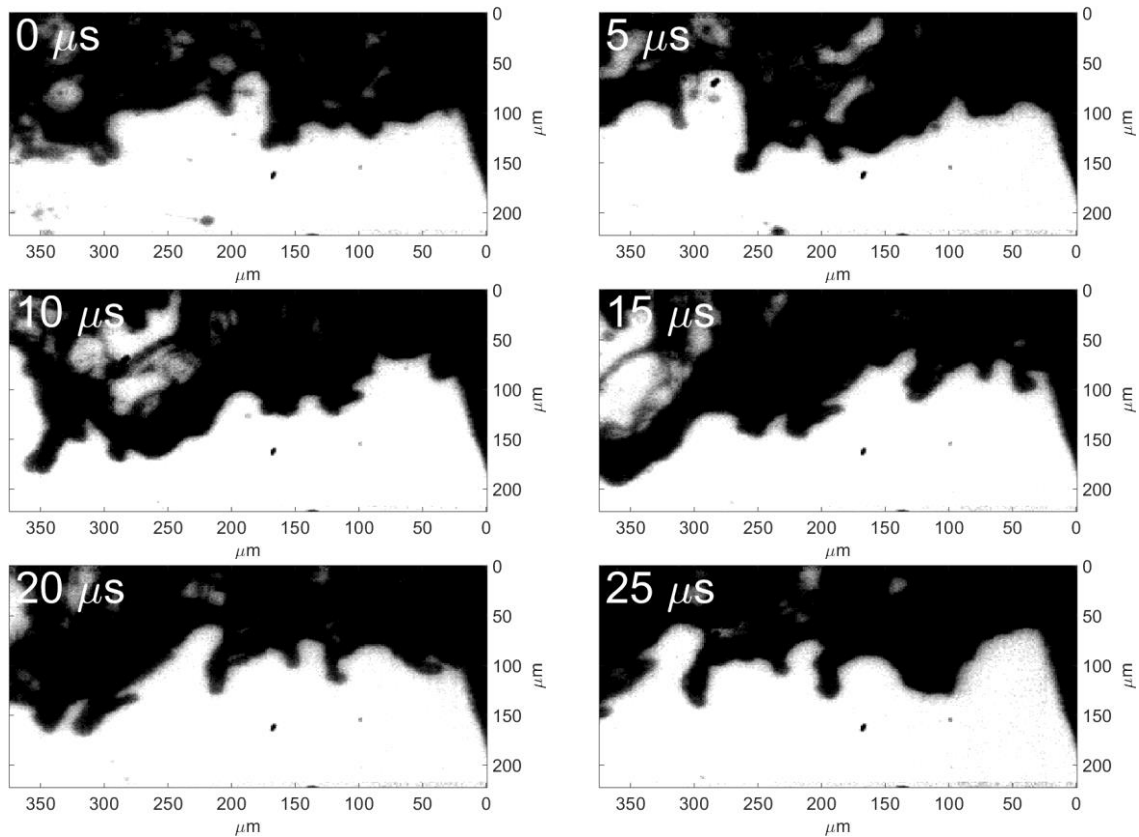


Figure 41: Microscopic images of the spray at 1.4 MPa (200 psi) injection pressure, 13.7x Magnification, 200 kfps framing rate and 90 ns exposure.

Higher temporal resolution imaging of the same spray at 480 kfps and 20 ns exposure are shown in Figure 42. However, these images are taken at reduced magnification of 2.9x since higher magnification is not possible at 480 kfps as explained earlier. These higher temporal resolution images were obtained to be able to better track the development of ligaments across frames.

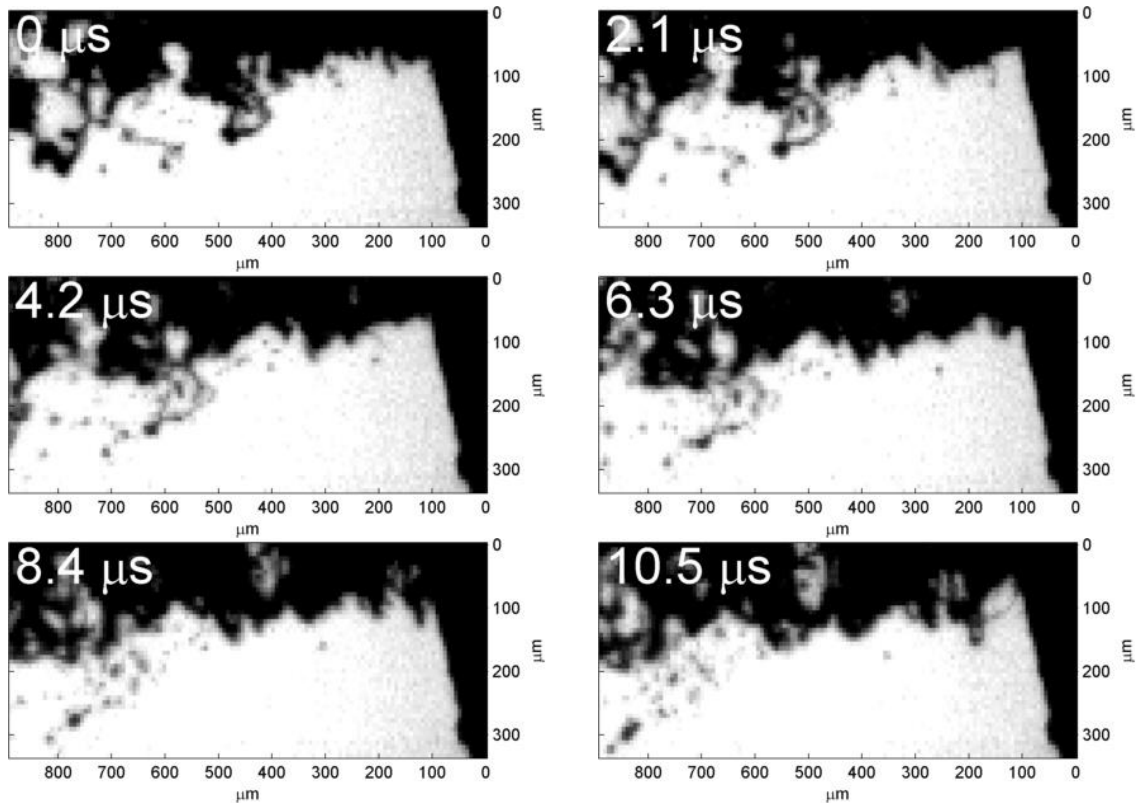


Figure 42: Microscopic images of the spray at 1.4 MPa (200 psi) injection pressure, 13.7x Magnification, 480 kfps framing rate and 20 ns exposure.

An effort was further made to take images at the 480 kfps acquisition rate in conjunction with the maximum magnification of 13.7x by exploiting the protective circuitry design of the LED driver. When the LED is driven above its limit of 1% duty, it flashes for a number of pulses before the protective circuitry of the driver kicks in and turns it off. We used these flashes to get 30 images at 480 kfps acquisition rate and maximum magnification with an exposure of 90 ns. The 90 ns exposure provided enough illumination for the maximum magnification case to distinguish between the spray and the background but also caused the LED to turn off after 30 flashes. A sequence of 6 images from these 30 is shown in Figure 43. The limitation of imaging either at maximum magnification or at higher framing rates in the previous images was removed by operating the LED driver in this configuration. The images provide simultaneous

spatial and temporal resolutions of $1.46 \mu\text{m}/\text{pixel}$ and 480 kfps respectively which significantly improves the tracking of features on the spray interface.

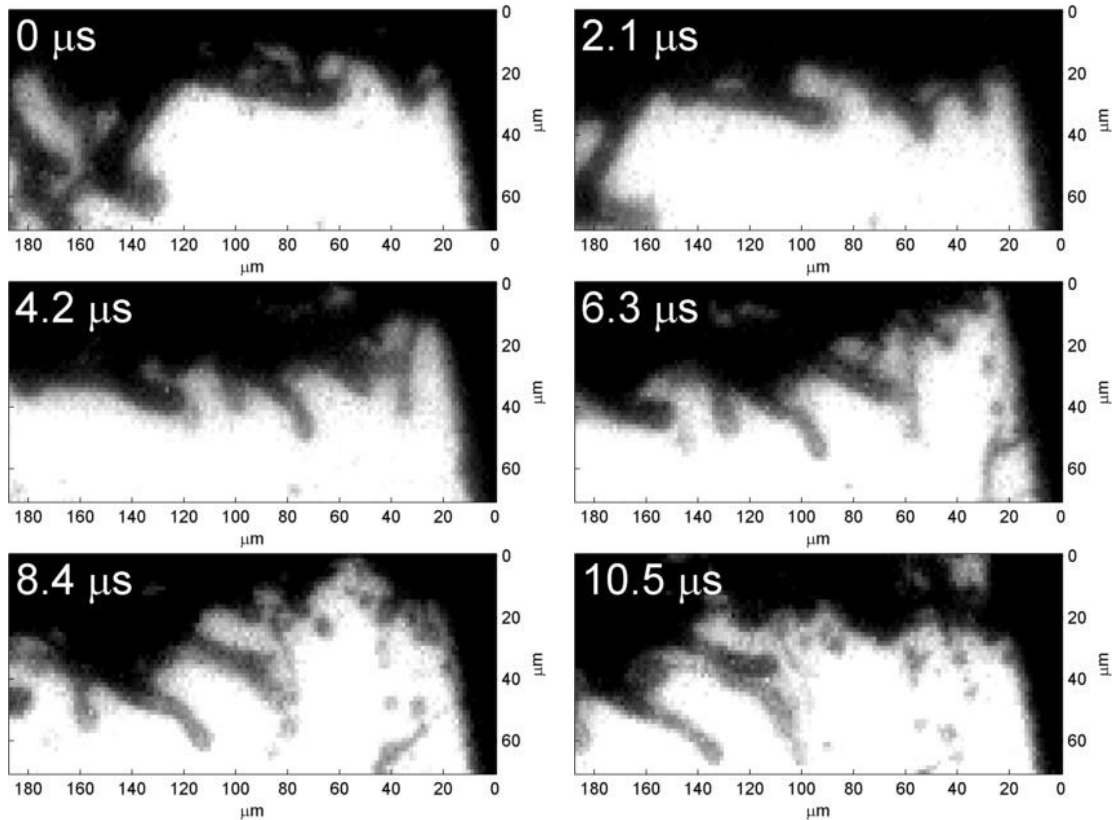


Figure 43: Microscopic images of the spray at 1.4 MPa (200 psi) injection pressure, 13.7x Magnification, 480 kfps framing rate and 90 ns exposure.

Back pressure testing was also performed at 1 MPa (10 bar) ambient pressure to see the effects of increased gas density on the ligament formation and propagation dynamics and also the size of droplets formed. A decrease in light throughput was experienced at higher pressures most likely because of the greater refractive index of the dense gases inside the combustion vessel which might have changed the light spot size on the imaging plane. A sequence of images at this back pressure and 1.4 MPa injection pressure is shown in Figure 44. It can be seen from these images that drop formation

occurs further upstream and the drop sizes are smaller as compares to the no back pressure case.

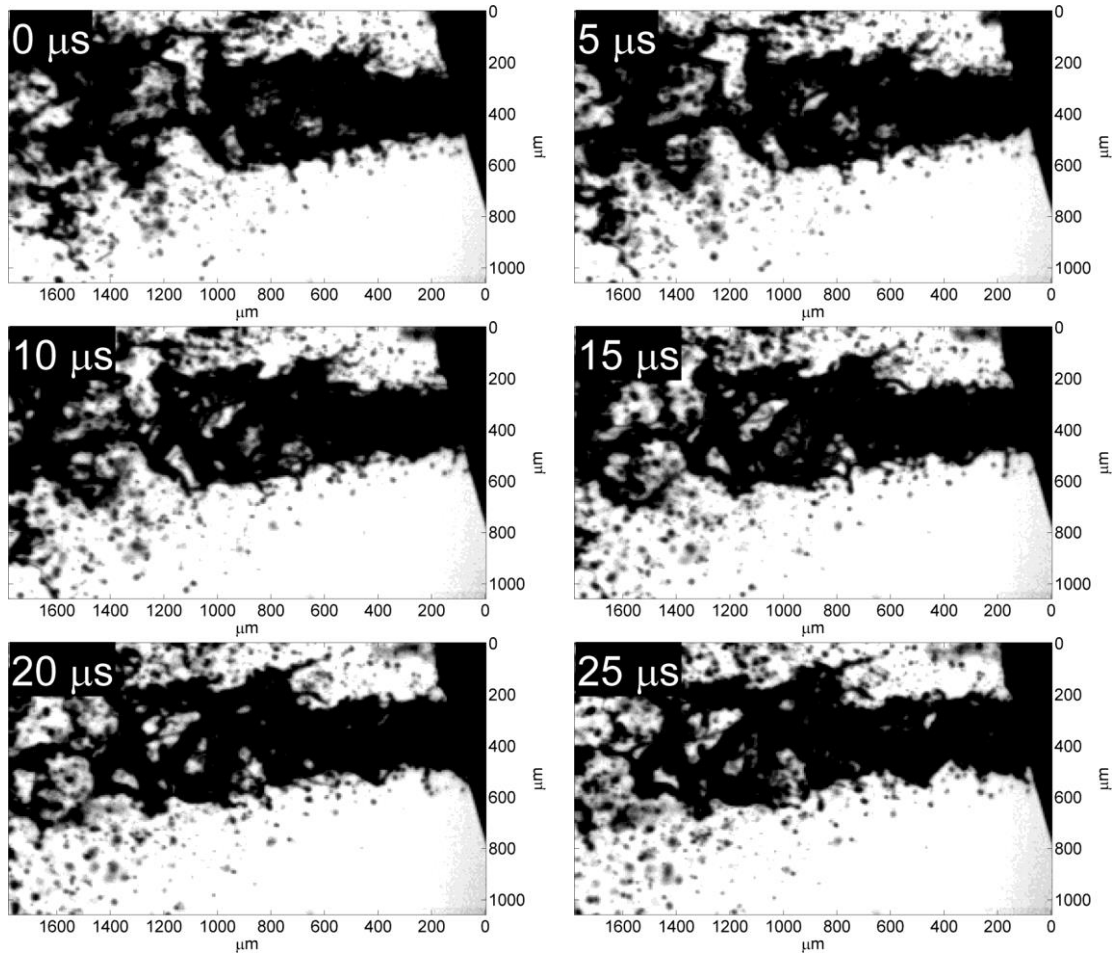


Figure 44: Microscopic images of the spray at 1.4 MPa (200 psi) injection pressure. 2.9x Magnification, 200 kfps framing rate and 90 ns exposure at 1 MPa ambient pressure

CHAPTER 5: CONCLUSIONS AND FUTURE WORK

The discussion of trade-offs inherent to high spatial and temporal resolution imaging showed that even with state of the art technologies, an optimization of the imaging system was required in order to achieve the resolutions required to image high pressure sprays. On the basis of these trade-offs, a high-speed microscopy imaging system has been optimized for high spatial and temporal resolution. The system employs a high-speed 1 MP camera at framing rates from 200 to 480 kfps, synchronized with a high-power pulsed LED illumination system and has magnification capabilities of 2.9x and 13.7x. The imaging resolution of the optical system was quantified which showed that it can resolve spatial frequencies of 72 lines/mm (13.88 μm) at 2.9x magnification and 102 lines/mm (9.80 μm) at 13.7x magnification. Measurement of the optical power at the imaging plane indicated a higher power for longer pulse durations which also caused a greater thermal load on the LED. Blur-free images were achieved at spatial resolution of 1.46 $\mu\text{m}/\text{pixel}$, simultaneously with a 200 kfps acquisition rate, and at 6.94 $\mu\text{m}/\text{pixel}$ with a 480 kfps acquisition rate. The system enabled imaging for the entire duration of an injection event (several milliseconds), offering significant improvements over historical spray atomization imaging data in the ability to track the temporal and spatial evolution of interface structures. In addition, the exploitation of the protective circuitry of the LED driver enabled the achievement of spatial resolutions of 1.46 $\mu\text{m}/\text{pixel}$ and temporal resolution of 480 kfps simultaneously, although it is only for 30 frames. This configuration represents the maximum capability of our optical system and the images

obtained with this configuration offer spatial and temporal resolutions which further add to the significantly improved resolution obtained by the normal LED operation.

The spray was imaged using exposures of 90 ns and 20 ns to see the effect of exposure duration on the capability to freeze the motion of the spray in the frame. The injection pressure of the spray was also varied to show how decreasing the speed of a spray improved its image in a frame and tracking the development of its features across successive frames. A spray injected at 3000 psi could not be frozen even at an exposure of 20 ns and low magnification of 2.9x. The intermediate pressure spray at 1000 psi was frozen in the frame with a 90 ns exposure and magnification of 2.9x but it was difficult to track its features across successive frames. The images of the low pressure spray at 200 psi showed a well-defined interface at a 90 ns exposure and the interfacial features were easily tracked from one frame to another. This injection pressure of 200 psi represents the condition of the spray which can be resolved using our designed system. The size of interfacial features and droplets observed by visual inspection in the images showed an increase in the size of features as the injection pressure of the spray was decreased which is consistent with theoretical predictions. The 13.7x magnification configuration enabled an optical resolution capability below 10 μm which was the expected size of the features for real (high pressure) fuel sprays but the low temporal resolution of 200 kfps and longer pulse duration of 90 ns restricted the resolution of features for a high pressure fuel spray.

Figure 45 shows the location of the 200 psi and the 3000 psi injection pressure spray at atmospheric back pressure on the regime plot of Figure 11 and compares it to the regime of sprays investigated in literature. We can see that the 200 psi spray which is

well resolved by our imaging system is in the 2nd Wind induced regime and the 3000 psi spray which cannot be resolved by our imaging system is in the atomization regime hence the capabilities of the system need to be further improved to image these real (high pressure) fuel sprays that lie in the atomization regime.

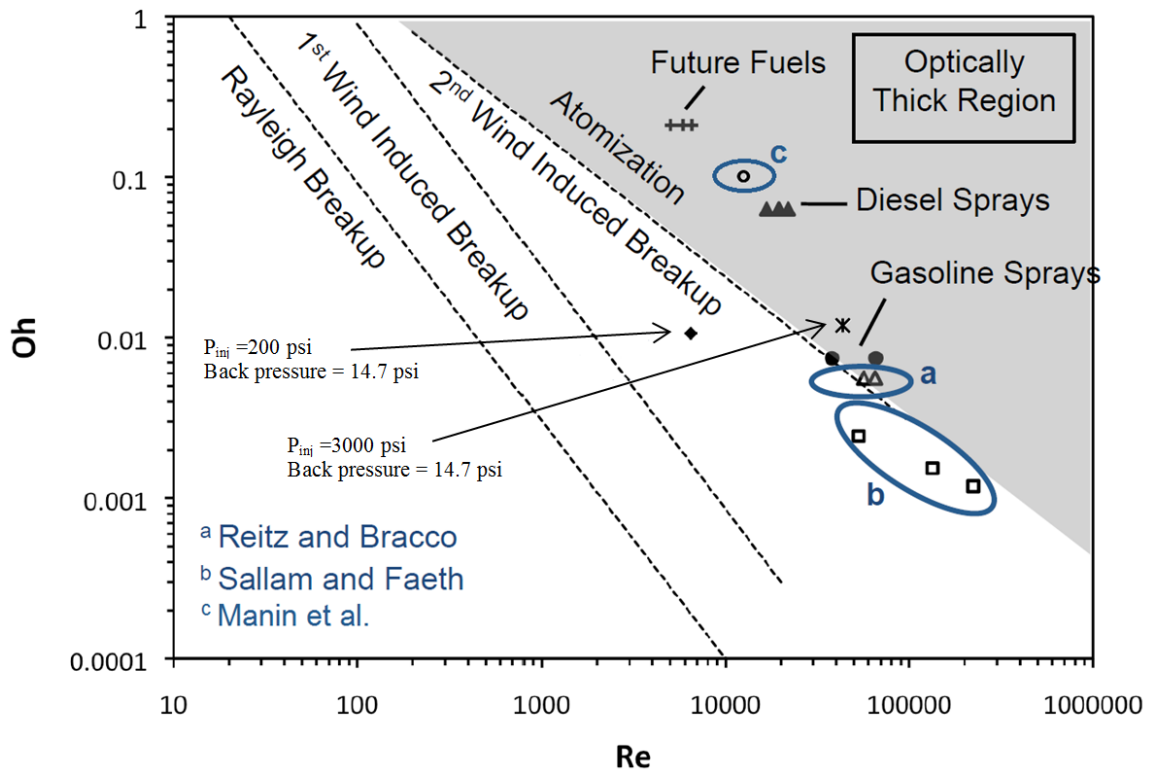


Figure 45: Comparison of sprays investigated in current work with sprays investigated in literature on the spray regime plot.

Future work will entail improving the system capabilities to resolve the features of high pressure fuel sprays. The proposed improvements in the system are to have shorter pulse widths (< 10 ns) and higher illumination at these pulse widths to be able to use faster framing rates. An improvement in the optical resolution is also required to resolve feature sizes smaller than $10 \mu\text{m}$ which might be present in high pressure fuel sprays. With rapidly improving LED technology, the LEDs are gradually getting faster

and brighter. These new generations of fast and bright LEDs will enable to have pulse width as short as 10 ns and will provide enough illumination to image at fast framing rates with sufficient contrast. Also a long-range microscope with a shorter working distance and a higher NA will help to collect more light and improve the MTF of the system. The optical resolution of the system can be improved by using a better quality microscopic lens such as the Infinity K2 DistaMax which offers a 1 μm resolution compared to 3 μm for the Questar QM-1. Statistical analyses of the plethora of data that we have obtained by this imaging system to quantitatively validate primary atomization models is also part of the proposed future work.

REFERENCES

- [1] US Energy Information Administration: International Energy Outlook 2014
http://www.eia.gov/oiaf/aeo/tablebrowser/#release=IEO2014&subject=1-IEO2014&table=15-IEO2014®ion=4-0&cases=Reference-2014_03_21.
[Accessed: 09-Feb-2015].
- [2] R. D. Reitz and F. V. Bracco, "Mechanism of atomization of a liquid jet," *Phys. Fluids*, vol. 25, no. 1982, pp. 1730–1742, 1982.
- [3] K.-J. Wu, R. D. Reitz, and F. V. Bracco, "Measurements of drop size at the spray edge near the nozzle in atomizing liquid jets," *Phys. Fluids*, vol. 29, no. 4, p. 941, 1986.
- [4] R. D. Reitz, "Modeling Atomization Processes In High Pressure Vaporizing Sprays," *At. Spray Technol.*, vol. 3, no. 4, pp. 309–337, 1987.
- [5] P. K. Wu, L. K. Tseng, and G. M. Faeth, "Primary Breakup in Gas/Liquid Mixing Layers for Turbulent Liquids," *At. Sprays*, vol. 2, no. 295–317, 1992.
- [6] P.-K. Wu and G. M. Faeth, "Aerodynamic Effects of Primary Breakup of Turbulent Liquids," *At. Sprays*, vol. 3, no. 3, pp. 265–289, 1993.
- [7] R. D. Reitz and F. B. Bracco, "On the Dependence of Spray Angle and Other Spray Parameters on Nozzle Design and Operating Conditions," in *SAE Technical Paper Series*, 1979.

- [8] J. M. Desantes, R. Payri, F. J. Salvador, and J. De la Morena, "Influence of cavitation phenomenon on primary break-up and spray behavior at stationary conditions," *Fuel*, vol. 89, no. 10, pp. 3033–3041, Oct. 2010.
- [9] M. A. Reddemann, F. Mathieu, D. Martin, and R. Kneer, "Impact of Physical Properties on Primary Breakup for a Diesel Nozzle Configuration," *At. Sprays*, vol. 21, no. 3, pp. 221–235, 2011.
- [10] K. A. Sallam and G. M. Faeth, "of Turbulent Liquid Jets in Still Air," vol. 41, no. 8, 2003.
- [11] S. Som and S. K. Aggarwal, "Assessment of Atomization Models for Diesel Engine Simulations," *At. Sprays*, vol. 19, no. 9, pp. 885–903, 2009.
- [12] K. a. Sallam, Z. Dai, and G. M. Faeth, "Liquid breakup at the surface of turbulent round liquid jets in still gases," *Int. J. Multiph. Flow*, vol. 28, no. 3, pp. 427–449, Mar. 2002.
- [13] K. . Sallam, Z. Dai, and G. . Faeth, "Drop formation at the surface of plane turbulent liquid jets in still gases," *Int. J. Multiph. Flow*, vol. 25, no. 6–7, pp. 1161–1180, Sep. 1999.
- [14] R. Reitz, "Computer modeling of sprays," *Spray Technol. Short Course, Pittsburgh, PA*, pp. 1–11, 1996.
- [15] C. Dumouchel, "On the experimental investigation on primary atomization of liquid streams," *Exp. Fluids*, vol. 45, no. 3, pp. 371–422, Jun. 2008.

- [16] C. Crua, T. Shoba, M. Heikal, M. Gold, and C. Higham, "High-speed microscopic imaging of the initial stage of diesel spray formation and primary breakup," *SAE Int.*, vol. 28, pp. 1085–1092, 2010.
- [17] T. Shoba, C. Crua, M. R. Heikal, and M. Gold, "Optical Characterisation of Diesel, RME and Kerosene Sprays by Microscopic Imaging," in *ILASS -- Europe 2011, 24th European Conference on Liquid Atomization and Spray Systems*, 2011, no. September, pp. 1–9.
- [18] L. M. Pickett, J. Manin, A. Kastengren, and C. Powell, "Comparison of Near-Field Structure and Growth of a Diesel Spray Using Light-Based Optical Microscopy and X-Ray Radiography," *SAE Tech. Pap. 2014-01-1412*, Apr. 2014.
- [19] J. Manin, M. Bardi, L. M. Pickett, R. N. Dahms, and J. C. Oefelein, "Microscopic investigation of the atomization and mixing processes of diesel sprays injected into high pressure and temperature environments," *Fuel*, vol. 134, pp. 531–543, 2014.
- [20] C. Badock, R. Wirth, A. Fath, and A. Leipertz, "Investigation of cavitation in real size diesel injection nozzles," *Int. J. Heat Fluid Flow*, vol. 20, no. 5, pp. 538–544, Oct. 1999.
- [21] <http://www.newport.com/Tutorial-Light-Collection-and-Systems-Throughput/381845/1033/content.aspx>.
- [22] <http://www.newport.com/Optics-Fundamentals/604533/1033/content.aspx>.